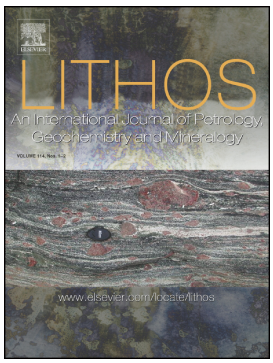

Platinum-group element and Au geochemistry of Late Archean to Proterozoic calc-alkaline and alkaline magmas in the Yilgarn Craton, Western Australia

Eunjoo Choi, Marco L. Fiorentini, Hannah S.R. Hughes, Andrea Giuliani

PII: S0024-4937(20)30353-4

DOI: https://doi.org/10.1016/j.lithos.2020.105716

Reference: LITHOS 105716

To appear in: *LITHOS*

Received date: 14 March 2020

Revised date: 23 July 2020

Accepted date: 27 July 2020

Please cite this article as: E. Choi, M.L. Fiorentini, H.S.R. Hughes, et al., Platinum-group element and Au geochemistry of Late Archean to Proterozoic calc-alkaline and alkaline magmas in the Yilgarn Craton, Western Australia, *LITHOS* (2020), https://doi.org/10.1016/j.lithos.2020.105716

Platinum-group element and Au geochemistry of Late Archean to Proterozoic calc-alkaline and alkaline magmas in the Yilgarn Craton, Western Australia

Eunjoo Choi[a,*] eunjoo.choi@research.uwa.edu.au, Marco L. Fiorentini[a], Hannah S.R Hughes[b,c], Andrea Giuliani[d,e]

[a]Centre for Exploration Targeting, School of Earth Sciences and ARC Centre of Excellence for Core to Crust Fluid Systems, University of Western Australia, 35 Stirling Highway, Crawley, WA 6009, Australia

[b]Camborne School of Mines, College of Engineering, Mathematics & Physical Sciences, University of Exeter, Penryn Campus, Penryn, Cornwall TR10 9FE, UK

[c]School of Geosciences, The University of Witwatersrand, 1 Jan Smuts Avenue, Braamfontein, 2000 Johannesburg, South Africa

[d]School of Earth Sciences, The University of Melbourne, Parkville, VIC 3010, Australia

[e]Institute of Geochemistry and Petrology, Department of Earth Sciences, ETH Zurich, Clausiusstrasse 25, Zurich 8092, Switzerland

[*]Corresponding author.

Abstract

The Yilgarn Craton of Western Australia is one of the largest Archean cratons in the world and is well-known for its metal endowment. In order to provide new insights into its metallogenic fertility and the nature of the upper mantle that lies underneath the craton, this study investigates the poorly constrained platinum-group element (PGE) and gold signatures of a selected suite of calc-alkaline lamprophyres, ultramafic lamprophyres, carbonatites and orangeites, ranging in age from the Proterozoic to the Late Archean. Proterozoic ultramafic lamprophyres and carbonatites within the Eastern Goldfields Superterrane (EGS) of the Yilgarn Craton have anomalously low PGE contents (Ir = 0.1-1.3 ppb; Ru = < 0.08 to 3.6 ppb; Rh = <0.04 to 0.4 ppb; Pt = <0.17 to 3.3 ppb; Pd = <0.12 to 4.4 ppb) and variable Au contents (<0.4 to 9.8 ppb). Based on their low PGE contents and unfractionated PGE patterns with $(Pd/Ir)_N$ ratios up to ~6, it is suggested that these magmas may derive from extremely low-degree partial melting of the convective mantle. Conversely, the Late Archean calc-

alkaline lamprophyres in the EGS exhibit comparatively fractionated PGE patterns with $(Pd/Ir)_N$ ratios up to ~27 and variable Au concentrations, including localised anomalous enrichments (up to 13.8 ppb). The fractionated PGE patterns are explained by incongruent melting of mantle sulfides with potential contribution from PPGE- and Au-bearing alloys, which would preferentially contribute Pt, Pd and Au over Ir, Ru and Rh. Combination of elevated Au and volatile contents in these rocks is consistent with derivation from a mantle source that was metasomatised by slab-derived fluids along a laterally extensive Late Archean subduction setting. This process may have provided a first-order control on the exceptional gold endowment of the Eastern Goldfields Superterrane.

Keywords: Platinum-group element; Gold; Calc-alkaline and alkaline magmatism; Yilgarn Craton; Late Archean; Proterozoic

1. Introduction

The Yilgarn Craton of Western Australia is one of the most gold-endowed geological regions in the world (Aitken et al., 2018; Barnes and Fiorentini, 2012; Blewett et al., 2010b). The gold (Au) and platinum-group elements (PGE) content of the mantle underlying the Yilgarn Craton is poorly constrained, and solely inferred from the signature of sub-alkaline mafic and ultramafic magmas (Barnes and Fiorentini, 2008; Fiorentini et al., 2010a, 2010b; Maier et al., 2009), which were mainly sourced from the convective mantle. However, multiple studies over the last decade suggested that the lithospheric mantle may be a primary source for Au and PGE (González-Jiménez et al., 2011, 2019; Griffin et al., 2013; Holwell et al., 2019; Hughes et al., 2017; Maier et al., 2012, 2017; Saunders et al., 2018; Tassara et al., 2017, 2018; Wang et al., 2020). Therefore, this study aims to establish the PGE and Au composition of the lithospheric mantle underneath the Yilgarn Craton, seeking any causative relationship with its exceptional Au endowment. In order to do so, we determined the concentrations of PGE and Au in selected Late Archean to Neoproterozoic calc-alkaline, alkaline and/or CO_2-rich mafic/ultramafic magmas from the Eastern Goldfields Superterrane, which is the most gold-endowed domain in the craton.

The examined samples include calc-alkaline lamprophyres (CAL), ultramafic lamprophyres (UML), carbonatites, orangeites (i.e. carbonate-rich olivine lamproites) and kimberlites, which commonly occur as small-volume sub-volcanic intrusions and related volcanic complexes in all cratons (e.g., Becker and Le Roex, 2006; Chalapathi Rao et al., 2011; Dawson, 1980; Foley, 2011; Giuliani and Pearson, 2019; Mitchell, 1995; Rock, 1986, 1991; Tappe et al., 2008). These rocks are characterised by elevated alkali (Na, K) and volatile (H_2O, CO_2) concentrations, as well as by a marked enrichment in incompatible trace elements (e.g., large-ion lithophile and rare earth elements). These features have been interpreted to reflect derivation from low-degree partial melting of the lithospheric mantle or upper asthenosphere (F < 10%; e.g., Brey et al., 2008; Dalton and Presnall, 1998; Dasgupta et al., 2009; Foley, 2008; Foley and Pintér, 2018; Giuliani and Pearson, 2019; Pearson et al., 2019).

Depletion in high-field strength elements (HFSE) combined with enrichment in volatiles and large-ion lithophile elements (LIL) in the CAL suggest derivation from a lithospheric mantle that was previously metasomatised by subduction-related fluids (e.g., Orozco-Garza et al., 2013; Pandey et al., 2018; Rock, 1984, 1991; Soder and Romer, 2018; van der Meer et al., 2016). Conversely, the observed radiogenic Sr combined with unradiogenic Nd and Hf isotope compositions of orangeites are typically attributed to lithospheric mantle sources that have experienced long-lived metasomatic enrichment (e.g., Chalapathi Rao et al., 2011; Coe et al., 2008; Kargin et al., 2014). On the other hand, moderately super-chondritic Nd and Hf isotope compositions in kimberlites may reflect asthenospheric or deeper sources (e.g., Choi, 2020; Nowell et al., 2004; Tappe et al., 2017; Woodhead et al., 2019). Finally, the petrogenesis of the UML is less clear and could involve asthenospheric and metasomatised lithospheric source components (Choi, 2020; Dalton et al., 2020; Tappe et al., 2008).

Combined with enriched gold contents in mantle xenoliths from numerous localities worldwide (Hughes et al., 2014; Maier et al., 2012; Saunders et al., 2018; Tassara et al., 2017), studies on gold geochemistry in calc-alkaline, alkaline and/or CO_2-rich ultramafic magmas have shown that the sub-continental lithospheric mantle (SCLM) is locally enriched in Au (Maier et al., 2017; McDonald et al., 1995; Wang et al., 2020; Zhang et al., 2010). Conversely, the role of the lithospheric mantle as a PGE source is still controversial, with the documentation of domains that are either depleted (Maier et al.,

2012, 2017; Tappe et al., 2017) or enriched (Chalapathi Rao et al., 2014; Hughes et al., 2016; McDonald et al., 1995; Zhang et al., 2010) in Pt and Pd. However, whereas in the past gold research mainly pertained to "hydrothermal" rocks and PGE studies would focus on "magmatic" suites, it is the integration of information on PGE and Au in mantle-derived magmas that may provide the most valuable constraints on the nature of the lithospheric mantle (Holwell et al., 2019; Hughes et al., 2014).

According to Choi et al. (2020), the Late Archean CAL from the Eastern Goldfields Superterrane (~2684-2640 Ma; McNaughton et al., 2005; Perring et al., 1989) were generated by melting of a source that had been metasomatised by subduction-related fluids. Choi et al. (2020) suggested that the juvenile radiogenic isotope signatures of these rocks is consistent with metasomatic enrichment occurring shortly prior to partial melting. Conversely, a comprehensive assessment of the origin of Paleoproterozoic UML, carbonatites and kimberlites in the EGS (~2025 Ma; Graham et al., 2004) established a common convective mantle source, reflected by circa-chondritic Sr-Nd-Hf isotope compositions (Choi, 2020). Furthermore, the enriched Sr-Nd-Hf isotope compositions of Mesoproterozoic orangeites from the Earaheedy Basin, along the northern margin of the Yilgarn Craton, may reflect the involvement of an ancient metasomatised lithospheric mantle source for these magmas (Choi, 2020). Here, we present the first study that integrates sulfur, PGE and Au geochemical data with previously reported petrographic, mineral chemistry and whole-rock major and trace-element results to provide a comprehensive assessment of the PGE-Au nature of low-volume, mantle-derived magmas in the Yilgarn Craton and its northern margin.

2. Geological setting

2.1. Archean geodynamic evolution of the Yilgarn Craton

The Yilgarn Craton mainly consists of metavolcanic and metasedimentary rocks, granitoid complexes and greenstone belts (Fig. 1), which formed principally between ~3050 and 2600 Ma, with minor >3.7 Ga components (e.g., Griffin et al., 2004; Myers, 1995; Pawley et al., 2012; Wilde et al., 1996). Based on stratigraphic, structural, geochemical and geochronological data, the craton has been

subdivided into the older Western Yilgarn Craton and younger Eastern Goldfields Superterrane (Cassidy et al., 2006). Between ~ 3.1-3.0 Ga, the Narryer, South West and Youanmi terranes in the Western Yilgarn Craton existed as separate lithospheric blocks, made up of reworked older crust (based on unradiogenic Hf isotope compositions; initial εHf -6.0 to -4.0; e.g., Cassidy et al., 2006; Mole et al., 2012, 2019). It is thought that after 2.8 Ga the Narryer and South West terranes have accreted to form the Youanmi Terrane (Cassidy et al., 2006; Myers, 1993; Nutman et al., 1993).

Geophysical and isotopic studies have shown that the lithosphere in the EGS is thinner and younger than the one in the Western Yilgarn Craton (e.g., Blewett et al., 2010b; Johnson et al., 2013; Mole et al., 2012, 2014, 2019; Wyche et al., 2012). From southwest to northeast, the EGS comprises the Kalgoorlie, Kurnalpi, Burtville and Yamarna terranes, which are joined by interconnected systems of crustal-scale NNW-trending faults (Fig. 1; Cassidy et al., 2006; Swager et al., 1997; Swager et al., 1992). The Kalgoorlie, Kurnalpi and Yamarna terranes contain ~2.72-2.66 Ga complexes, varying from ultramafic to felsic compositions (Barley et al., 2003; Barley et al., 2002; Pawley et al., 2007; Pawley et al., 2012; Swager et al., 1997), which include the minor CAL intrusions that are the subject of this study (Choi et al., 2020; Perring et al., 1989; Taylor et al., 1994). The occurrence of these lamprophyres combined with the calc-alkaline affinity of widespread felsic to intermediate igneous rocks in the Kalgoorlie and Kurnalpi terranes could indicate a Late Archean subduction event in the region (Choi et al., 2020), even though other authors have suggested a plume origin for these magmas (e.g., Barnes and Van Kranendonk, 2014; Smithies et al., 2018b). The Burtville Terrane contains 2.96-2.77 Ga successions of intermediate and felsic volcanic rocks, sharing lithological and temporal affinities with the Youanmi Terrane in the Western Yilgarn Craton (Pawley et al., 2007; Pawley et al., 2012).

After ~2.7 Ga both the western and eastern portions of the Yilgarn Craton display comparable geological features, such as the presence of widespread coeval felsic magmas with similar geochemical and isotopic characteristics (Cassidy et al., 2006), as well as the cessation of any komatiitic activity (e.g., Mole et al., 2013; Pidgeon and Wilde, 1990). Craton-wide felsic magmatism from 2.65 to 2.62 Ga is thought to reflect the cratonisation of the Yilgarn Craton into its current form (Cassidy et al., 2006; Czarnota et al., 2010; Kent et al., 1996; Mole et al., 2014).

2.2. Proterozoic evolution of the Yilgarn Craton

The northern margin of the Yilgarn Craton and the southern margin of the Pilbara Craton experienced at least three Proterozoic orogenic events. The Ophthalmia Orogeny occurred between 2.215 and 2.145 Ga, when the south margin of the Pilbara Craton collided with the Glenburgh Terrane (e.g., Johnson et al., 2011; Occhipinti et al., 2017). Subsequently, the combined Glenburgh Terrane and Pilbara Craton accreted to the northern margin of the Yilgarn Craton during the Glenburgh Orogeny between 2.005-1.950 Ga (Johnson et al., 2011). It is thought that the Earaheedy Basin, which formed at this time as a pro-foreland basin to the Glenburgh Orogen (Sheppard et al., 2016), continued to subside until ~1.8 Ga, when the Yilgarn and Pilbara cratons collided during the Capricorn Orogeny (Johnson et al., 2011; Roche et al., 2017; Sheppard et al., 2016). In the Earaheedy Basin, orangeite pipes were emplaced at ca. 1.9-1.7 Ga in Nabberu (Shee et al., 1999). In contrast, the south-eastern margin of the Yilgarn Craton was affected by the Albany Fraser Orogeny, which occurred in two stages of continental collision: Stage I (1330-1260 Ma) and Stage II (1225-1140 Ma), followed by intracratonic reactivation with high-grade metamorphism and extensive granitic magmatism (Clark et al., 2000; Kirkland et al., 2011; Nelson et al., 1995; Spaggiari et al., 2014; Spaggiari et al., 2015).

The Yilgarn Craton and its margins record geological evidence of multiple post-Archean broad-scale magmatic events. The Widgiemooltha mafic dykes intruded pervasively across the Yilgarn Craton at ~2.42 Ga (Nemchin et al., 1994; Pisarevsky et al., 2015; Smirnov et al., 2013). A widespread ~2.06 Ga alkaline province within the EGS includes UML, carbonatites and minor kimberlites (Choi, 2020), which are the subject of this study. Occurrences of ~1.4-1.3 Ga orangeites at Bulljah and Jewill within the Earaheedy Basin have been inferred to be associated with extensional tectonics and rifting following the breakup of the Columbia supercontinent (Choi, 2020; Choi et al., in revision). Another prominent post-Archean dyke swarm is the ~1.21 Ma Marnda Moorn Large Igneous Provinces (LIP), which is considered to be related to breakup of the Columbia supercontinent (e.g., Wang et al., 2014). At ~1.070-1.065 Ga, the extensive but short-lived Warakurna LIP was

emplaced as a series of mafic intrusions across the northern Yilgarn Craton (e.g., Wingate et al., 2004). The emplacement of UML at Norseman in the southern EGS (~863 Ma; Robey et al., 1989) could be related to the extensional regime that followed Rodinia breakup (Choi, 2020).

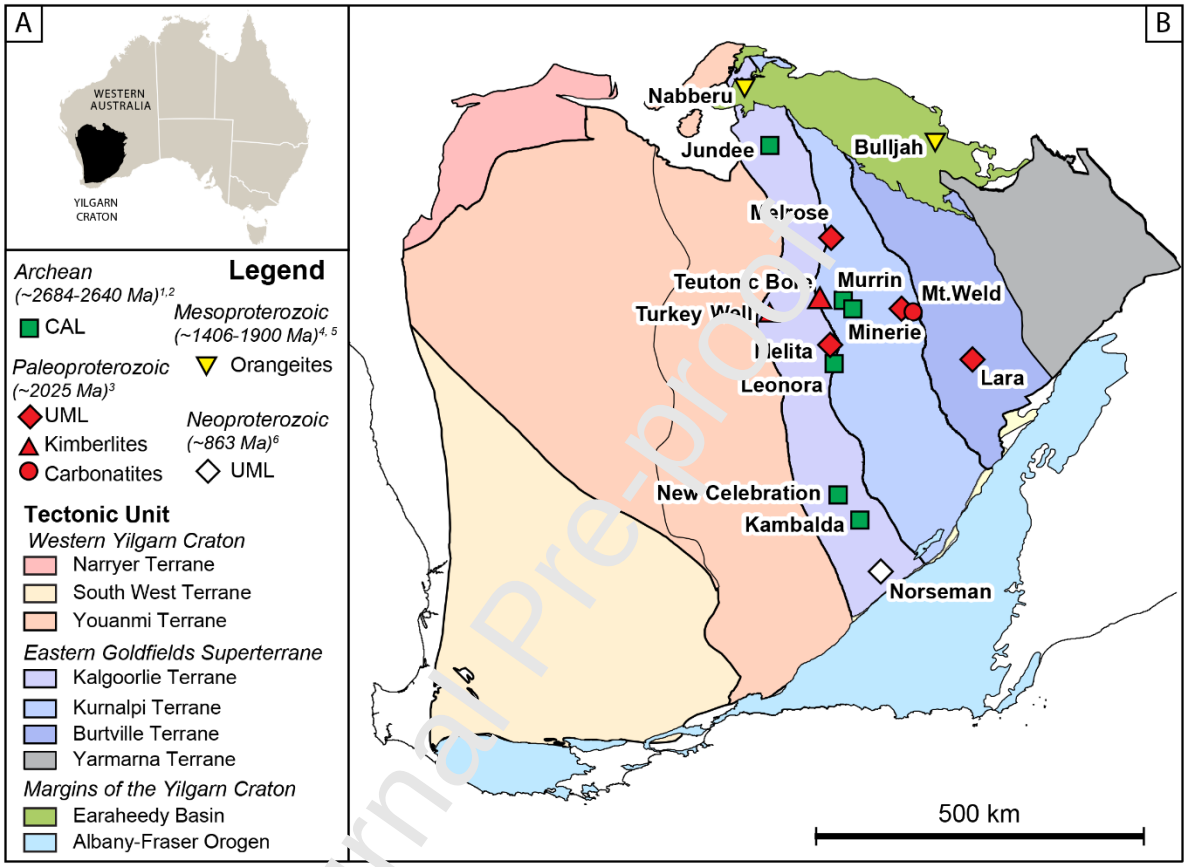

Fig. 1 A) Location of the Yilgarn Craton in Australia. (B) Simplified geological map of the Yilgarn Craton, showing distribution of CAL, UML, carbonatites, orangeites and kimberlites. The emplacement ages of the collected samples are from [1]Perring (1989), [2]McNaughton et al. (2005), [3]Graham et al. (2004), [4]Choi (2020), [5]Shee et al. (1999), and [6]Robey et al. (1989).

3. Samples and analytical methods

A total of 35 rock samples from 15 different localities within and along the northern margin of the Yilgarn Craton were analysed for PGE and Au geochemistry, including CAL, UML, carbonatites, orangeites and kimberlites. The samples were sourced from the archives of the University of Western

Australia (UWA), the Core Library of the Geological Survey of Western Australia (GSWA), and directly from researchers who have previously worked in the area (Stuart Graham, Mark Mitchell) with additional samples from the locality of Jundee provided by Northern Star Resources. Based on the localities and emplacement ages shown in Figure 1, the rocks are divided into four groups:

1) Late Archean *calc-alkaline lamprophyres* (CAL) from Kambalda, New Celebration, Leonora, Minerie, Murrin and Jundee in the Eastern Goldfields Superterrane. Previous studies of these and other similar CAL from this area (Currie and Williams, 1993; Perring et al., 1989; Taylor et al., 1994) reported that these magmas were contemporaneous with mafic dykes that cut the Paringa Basalt (the uppermost unit in the Kambalda Sequence 2720-2680 MaSaid and Kerrich, 2009), and traversed by felsic porphyries with an age of 2660 ± 4 Ma (Compston et al., 1985). These observations, combined with an unpublished zircon U-Pb age of 2684 ± 6 Ma reported in Perring et al. (1989) and U-Pb ages of hydrothermal zircon and monazite at the Golden Mile Deposit of 2642 ± 6 Ma and 2637 ± 20 Ma, respectively (McNaughton et al. (2005), constrain the CAL emplacement age to be between ~2684-2640 Ma. The CAL display porphyritic textures and contain phenocrysts of hastingsite or hornblende (calcic amphibole), minor clinopyroxene and biotite in a fine-grained groundmass dominated by albitic feldspar. Orthopyroxene and feldspar phenocrysts are notably absent. These features are identical to those of global CAL (Rock, 1991). The CAL experienced regional greenschist-facies metamorphism as indicated by widespread feldspar albitisation and formation of locally abundant actinolite amphibole and chlorite at the expenses of calcic amphibole and biotite, respectively. Secondary pyrite is observed in several samples from Jundee and Kambalda.
2) Paleoproterozoic *alkaline ultramafic magmas* in the Eastern Goldfields Superterrane, including UML, carbonatites, and kimberlites. The UML and carbonatites from the same locations of this study were previously dated using Re-Os isotopes, which provided an emplacement age of 2025 ± 10 Ma for this alkaline province (Graham et al., 2004). A petrographic summary of these Paleoproterozoic rock types from the EGS is listed below:

a) UML at Lara, Melrose Akbar, Melita, and Granny Smith: The UML samples are porphyritic and contain abundant phenocrysts of phlogopite and serpentinised olivine, in a groundmass of phlogopite, clinopyroxene and minor carbonate. These UML are classified as *aillikites* based on the absence of melilite, feldspars and feldspathoids in the groundmass (Tappe et al., 2005). Rare partially resorbed clinopyroxene macrocrysts (up to 5 mm) in the UML from Lara are considered to be xenocrysts. Secondary pyrite occurs in samples from Lara, but no sulfides were observed in thin sections of the other samples.

b) Carbonatites at Mt Weld: They contain apatite, phlogopite, magnetite, olivine, pyrochlore, rare occurrences of secondary pyrite and have > 50 vol.% calcite.

c) Kimberlites at Teutonic Bore and Turkey Well. These samples have previously been classified as kimberlites, based on their macrocrystic components (Graham et al., 2004; Kiviets et al., 1998). These rocks are mainly composed of serpentine, calcite, magnetite and altered perovskite with secondary pyrite associated with extensive alteration and replacement assemblages (silicification, serpentinisation and carbonation).

3) Mesoproterozoic *orangeites* (also known as Group II kimberlites, or recently "African lamproites"; Mitchell, 1995; Scott-Smith et al., 2018) from the Earaheedy Basin along the northern margin of the Yilgarn Craton, including Nabberu (~1700-1900 Ma; based on stratigraphic relationships; Shee et al., 1999) and Bulljah (1406 ± 10 Ma; Rb-Sr mica age; Choi, 2020). The samples from Bulljah are classified as orangeites based on the presence of abundant phlogopite phenocrysts in a groundmass of abundant phlogopite and lesser titanite (probably after perovskite), spinel, magnetite, and calcite with minor apatite, quartz and pyrite. The orangeites from Nabberu are highly altered consisting predominantly of serpentine and chlorite with occasional phlogopite remnants, minor calcite, magnetite, and altered perovskite.

4) One Neoproterozoic UML sample from Norseman (863 ± 9 Ma; mica Rb/Sr; Robey et al., 1989), in the southern part of the EGS. Its petrographic features are similar to those of the UML from the EGS.

Details of petrography, mineral chemistry of key silicate and oxide phases as well as whole-rock major, minor element and radiogenic isotope geochemistry for the calc-alkaline and alkaline ultramafic rocks investigated in this study were previously reported in Choi (2020) and Choi et al. (2020).

3.1. Analytical methods

Whole-rock PGE, Au and S concentrations were determined on rock powders prepared in an agate mill. All samples were analysed at the Geoscience Laboratories of the Ontario Geological Survey in Sudbury, Canada. Platinum-group element and Au data were generated with the conventional nickel sulfide (NiS) fire-assay pre-concentration technique followed by tellurium co-precipitation and ICP-MS analysis. Assessment of quality and reproducibility was undertaken by replicate analyses of TDB-1, WPR-1, WGB-1, WMG-1 and an in-house standard of komatiite, with lowest concentration levels (i.e. detection limits) of 0.01 ppb for Ir, 0.08 ppb for Ru, 0.04 ppb for Rh, 0.17 ppb for Pt, 0.12 ppb for Pd, and 0.4 ppb for Au. Analytical details for all the techniques utilised to generate the PGE data in this study, including sample preparation, accuracy, and precision have been described by Barnes and Fiorentini (2008) and Fiorentini et al. (2010a). These authors also provide information on internal and inter-laboratory reproducibility and sample homogeneity. Total sulfur contents were measured by infrared absorption after combustion in an oxygen-rich environment oxidises sulfur, with a detection lower limit of 0.003 wt.%. Further details are available at www.mndm.gov.on.ca/sites/default/files/2018_geo_labs_brochure.pdf.

4. Results

4.1. Sulfur contents

Sulfur contents in the full sample suite are variable from below detection limit (0.003 wt.%) to 0.87 wt.%. Most CAL samples contain S contents < 0.10 wt.% (n = 12; Table 1), with three samples having more than 0.20 wt.%. Among the UML, two samples from Lara have high S contents of 0.25 and 0.87 wt.%, whereas three samples from the EGS contain < 0.01 wt.%. Sulfur content in the only

UML sample analysed from Norseman is 0.04 wt.%. The Mt. Weld carbonatites have highly variable S contents between 0.01 and 0.73 wt.% (n = 4). Orangeites from the Earaheedy Basin show a relatively narrow range of very low sulfur concentrations (<0.04 wt.%; n = 3). The two highly altered kimberlite samples from the EGS (Turkey Well and Teutonic Bore) contain ~0.05 wt.% S. The very low S contents in the calc-alkaline and alkaline ultramafic samples investigated in this study are reflected in the presence of only very minor amounts of sulfides, which mainly occur as secondary pyrite (Choi, 2020; Choi et al., 2020).

4.2. PGE and Au geochemistry

4.2.1. Calc-alkaline lamprophyres

The examined CAL have low Ir (<0.01 to 0.3 ppb; n = 19; Table 1) and Ru contents (≤ 0.4 ppb, and below the detection limit of 0.08 ppb in more than half of the CAL samples), with moderately low Rh contents (0.1-0.3 ppb). Palladium, Pt and Au contents in the CAL exhibit large variability, from 0.8 to 4.7 ppb, 1.0 to 4.3 ppb, and 0.4 to 13.8 ppb, respectively. Primitive-mantle normalised PGE patterns show strong fractionation (Fig. 2A), with highly variable $(Pd/Ir)_N$ ratios from 3.4 to 26.6, and a more restricted range in $(Pd/Pt)_N$ ratios from 0.4 to 2.4. These patterns also display negative Ru anomalies and strong positive Au anomalies. Compared to the other rock types in this study, the CAL exhibit lower Ir, and Ru and higher Pt and Au contents. The CAL samples show a positive correlation between Ir and MgO concentrations (Fig. 3A), and a broad positive trend between Ir (or, to a lesser extent, Ru and Rh) and Cr (Fig. 4D). In general, Ir contents have positive correlations with other PGEs (Fig. 5). The new PGE data presented in this study are broadly similar to those found in Cenozoic CAL from China (Gan and Huang, 2017).

The new data from the CAL in the Yilgarn Craton presented here show lower Pt, Pd and Au contents than values previously reported by Taylor et al. (1994) from similar localities in the Eastern Goldfields Superterrane. These authors used NiS pre-concentration techniques followed by ICP-MS to analyse all PGE; they carried out additional Pd and Pt determinations for the same samples using Pb-fire assay pre-concentration methods followed by graphite-furnace atomic absorption spectrometry

(GFAAS). There was poor agreement between the two methods used by Taylor et al. (1994) due to low analytical precision for Pd contents. The study also used ICP-MS, GFAAS, instrumental neutron activation (INAA), and radiochemical NAA (RNAA) methods for Au contents, showing relatively narrow confidence limits for very high Au samples (> ~1000 ppb), whereas samples with lower Au contents (<100 ppb) were characterised by poor covariance between these methods. The analytical techniques employed in Taylor et al. (1994) may have hampered the precise determination of Pt, Pd and Au contents, showing anomalously high values that may not reflect accurate natural concentrations.

4.2.2. Ultramafic lamprophyres

The UML from the EGS contain variable Ir (< 0.01 to 1.3 ppb; n = 5; Table 1), Ru (0.1-3.6 ppb) and Pd (0.2-4.4 ppb) contents, with moderate Pt values (0.7-3.3 ppb). The Rh and Au concentrations vary from 0.1 to 0.4 ppb and 0.6 to 2.7 ppb, respectively; these values are lower than those detected in the CAL analysed in this study. Primitive mantle normalised PGE patterns of the UML (Fig. 2B) generally exhibit moderate fractionation with relatively narrow ranges of $(Pd/Ir)_N$ of 1.0-5.5 and $(Pd/Pt)_N$ of 0.3-1.5. Similar patterns are also observed in kimberlites from the Karelian Craton (Maier et al., 2017) and the Kaapvaal Craton (McDonald et al., 1995). A UML sample from Melita (Melita 1 pipe) contains higher total PGE contents (14 ppb) than the other UML samples (up to 4 ppb), but shows a flat PGE pattern similar to the EGS kimberlite samples. The PGE patterns of the UML from the EGS exhibit strong positive Au anomalies compared to other alkaline samples in this study. The UML samples from this study exhibit positive correlations of Ir, Ru, and Rh with Ni and Cr contents (Fig. 4). Their Ir contents have positive trends with Ru and Rh, but are not correlated to Pd and Pt (Fig. 5).

The UML sample from Norseman contains similar PGE contents to the UML from the Eastern Goldfields Superterrane. However, this sample contains much higher Au (9.8 ppb; Table 1; Fig. 2B) than the other alkaline rock samples investigated in this study, as well as compared to global orangeites and kimberlites (Maier et al., 2017; McDonald et al., 1995). Similarly to the UML sample

from Lara in the EGS, the primitive mantle-normalised PGE pattern of the Norseman UML reveals a less fractionated signature, with a low $(Pd/Ir)_N$ ratio of 3.6.

4.2.3. Carbonatites

Carbonatites from the Mt. Weld locality contain very low concentrations of Ir and Pd-platinum group elements (PPGE; Rh, Pt and Pd), with Ir ≤ 0.1 ppb, Pt = 0.7-1.2 ppb and Pd = 0.3-0.8 ppb (n = 4; Table 1). Ruthenium and Rh contents in the carbonatites are generally below detection limits. Two carbonatite samples contain Au contents above detection limits (0.[illegible] and 3.7 ppb, respectively). The $(Pd/Ir)_N$ and $(Pd/Pt)_N$ ratios in the carbonatites are up to 3.4 and 1.1, respectively, which are within the range of the UML from the EGS.

4.2.4. Orangeites

Orangeite samples from Bulljah and Nabberu in the Earaheedy Basin contain higher Ir (0.3-1.1 ppb; n = 4) and Ru (0.7-2.1 ppb) concentrations than those in the other samples in this study, whereas their Rh, Pt and Pd contents are low (0.1-0.2 ppb; 0.2-1.5 ppb; and 0.2-0.9 ppb, respectively). Only one sample from Bulljah has Au content above the limit of detection (3.8 ppb). In general, the Bulljah orangeites contain similar PGE contents to orangeites from the Karelian Craton (Maier et al., 2017), but are lower than orangeites from the Bastar Craton (Chalapathi Rao et al., 2014) and Kaapvaal Craton (McDonald et al., 1995). The relatively high PGE levels from McDonald et al. (1995) could reflect the lower precision of the INAA method and the heterogeneity of the standard used, as discussed by Maier et al. (2017).

The orangeites from Bulljah exhibit relatively flat primitive mantle-normalised PGE patterns similar to those of the UML, whereas the orangeites from Nabberu display negative slopes. The orangeites from both Bulljah and Nabberu show low $(Pd/Ir)_N$ ratios (0.1-0.7) compared to the CAL, UML and carbonatites investigated in this study (Fig. 2D). The $(Pd/Pt)_N$ ratios of the Nabberu samples are 0.3 and 1.1, whereas the Bulljah samples show a $(Pd/Pt)_N$ ratio of 0.2, which is the lowest of the entire sample suite. A strong positive Au anomaly is observed in sample BJ5-1 from Bulljah.

4.2.5. Kimberlites

A kimberlite sample from Teutonic Bore in the Eastern Goldfield Superterrane shows contents below detection limit for all PGE except Ir (0.01 ppb). In contrast, one kimberlite sample from Turkey Well exhibits very high PGE contents (Ir = 1.3 ppb, Ru = 3.1 ppb, Rh = 0.4 ppb, Pd = 4.8 ppb, and Pt = 2.8 ppb) compared to the other samples in this study, with $(Pd/Ir)_N$ and $(Pd/Pt)_N$ ratios of 1.9 and 1.8. Its Au content is below the detection limit (0.4 ppb). In general, the PGE contents in the Turkey Well kimberlite are similar to those found in kimberlites from the Kaapvaal and North China cratons (McDonald et al., 1995; Zhang et al., 2010), but slightly higher than PGE contents in kimberlites from the Karelian, Superior and Kaapvaal cratons (Maier et al., 2017; Tappe et al., 2017). The primitive mantle-normalised PGE pattern of the Turkey Well kimberlite is similar to those of global kimberlites and less fractionated compared to the other samples in this study (Fig. 2E).

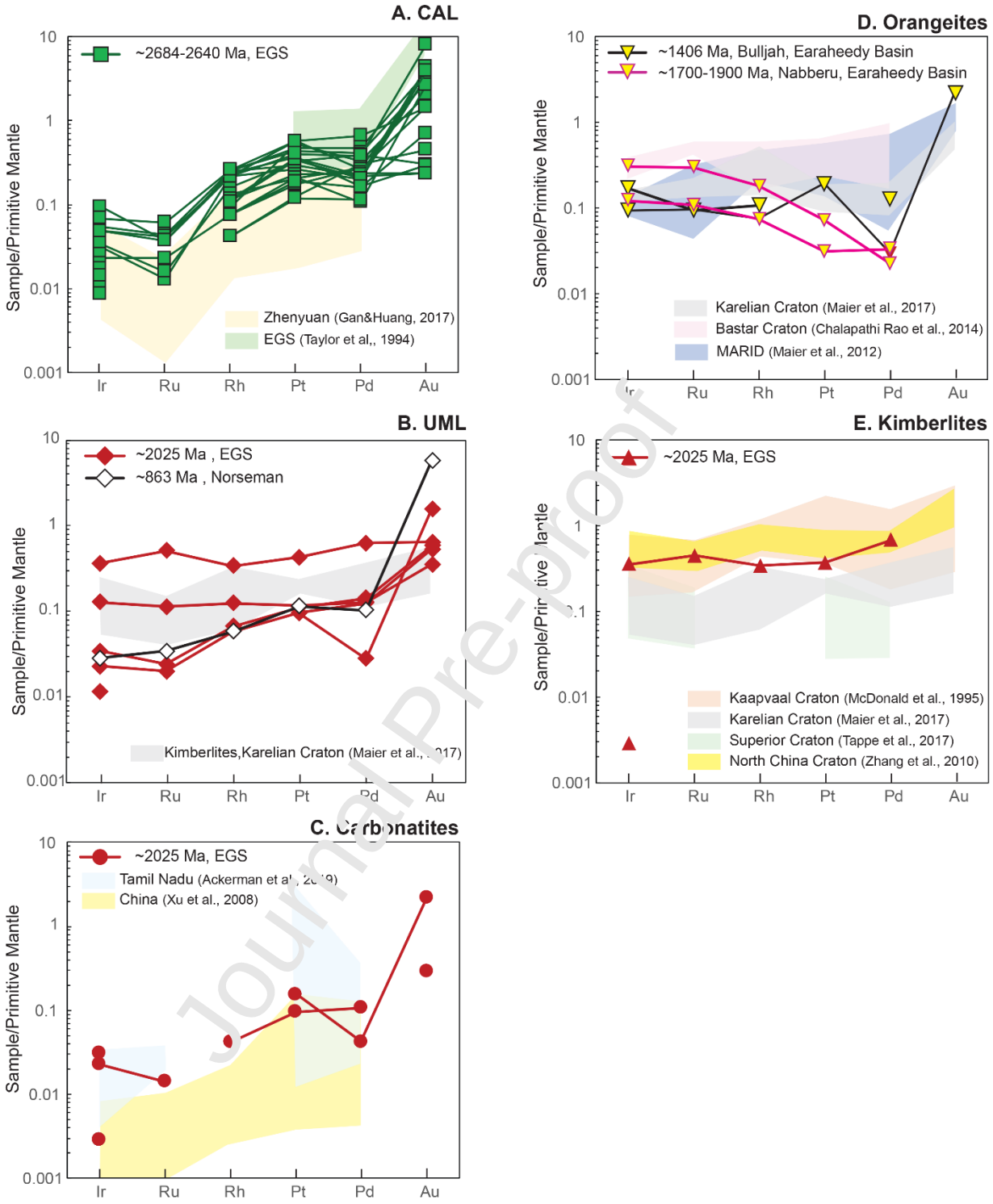

Fig. 2 Primitive mantle-normalised PGE-Au patterns for (A) CAL from the EGS, (B) UML from the EGS, including Norseman, (C) the Mt. Weld carbonatites, (D) the Earaheedy Basin orangeites, and (E) kimberlites from the EGS. Normalisation values for PGE and Au are from Day et al. (2016) and references therein.

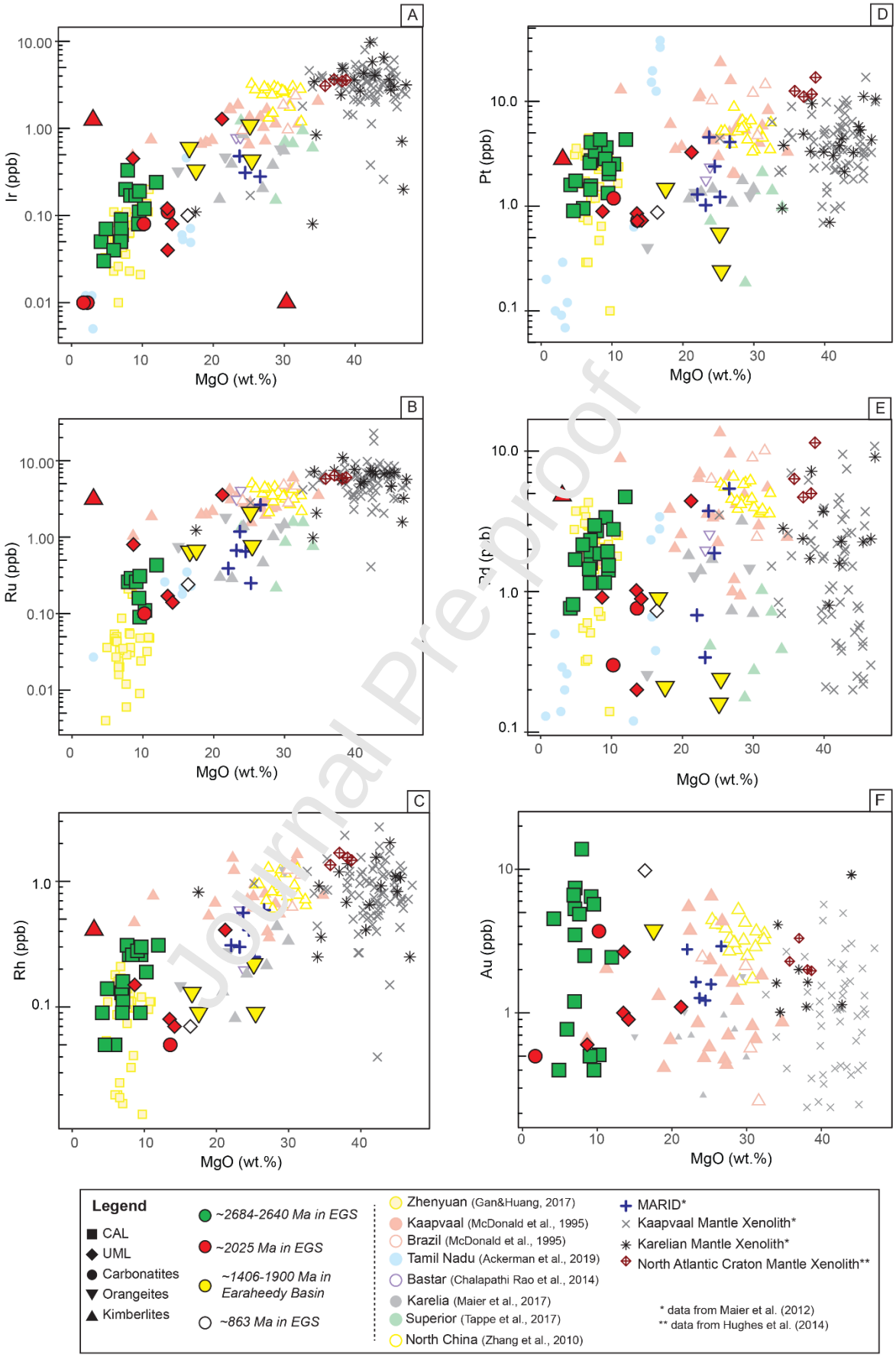

Fig. 3 Platinum-group element (ppb) versus MgO (wt.%) content for CAL, UML, carbonatites, orangeites and kimberlites from the Yilgarn Craton and selected localities globally. Data for mantle xenoliths are shown for comparison.

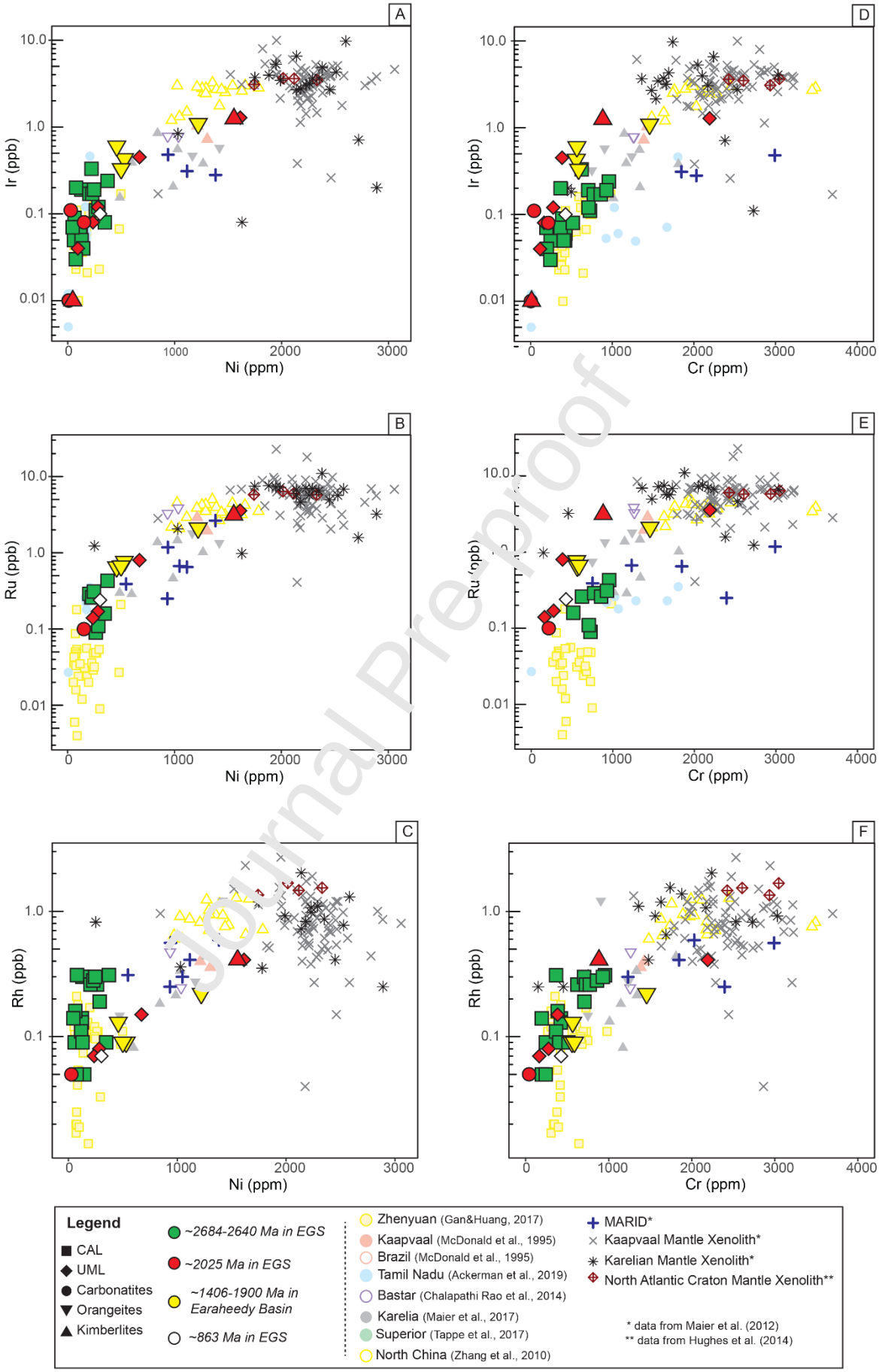
A
Ir (ppb)
Ni (ppm)
D
Ir (ppb)
Cr (ppm)
B
Ru (ppb)
Ni (ppm)
E
Ru (ppb)
Cr (ppm)
C
Rh (ppb)
Ni (ppm)
F
Rh (ppb)
Cr (ppm)
Legend
CAL
UML
Carbonatites
Orangeites
Kimberlites
~2684-2640 Ma in EGS
~2025 Ma in EGS
~1406-1900 Ma in Earaheedy Basin
~863 Ma in EGS
Zhenyuan (Gan&Huang, 2017)
Kaapvaal (McDonald et al., 1995)
Brazil (McDonald et al., 1995)
Tamil Nadu (Ackerman et al., 2019)
Bastar (Chalapathi Rao et al., 2014)
Karelia (Maier et al., 2017)
Superior (Tappe et al., 2017)
North China (Zhang et al., 2010)
MARID*
Kaapvaal Mantle Xenolith*
Karelian Mantle Xenolith*
North Atlantic Craton Mantle Xenolith**
* data from Maier et al. (2012)
** data from Hughes et al. (2014)

Fig. 4 Iridium, Ru and Rh (ppb) versus (A-C) Ni (ppm) and (D-F) Cr (ppm) concentrations for CAL, UML, carbonatites, orangeites and kimberlites from the Yilgarn Craton and selected localities globally. Data for mantle xenoliths are shown for comparison.

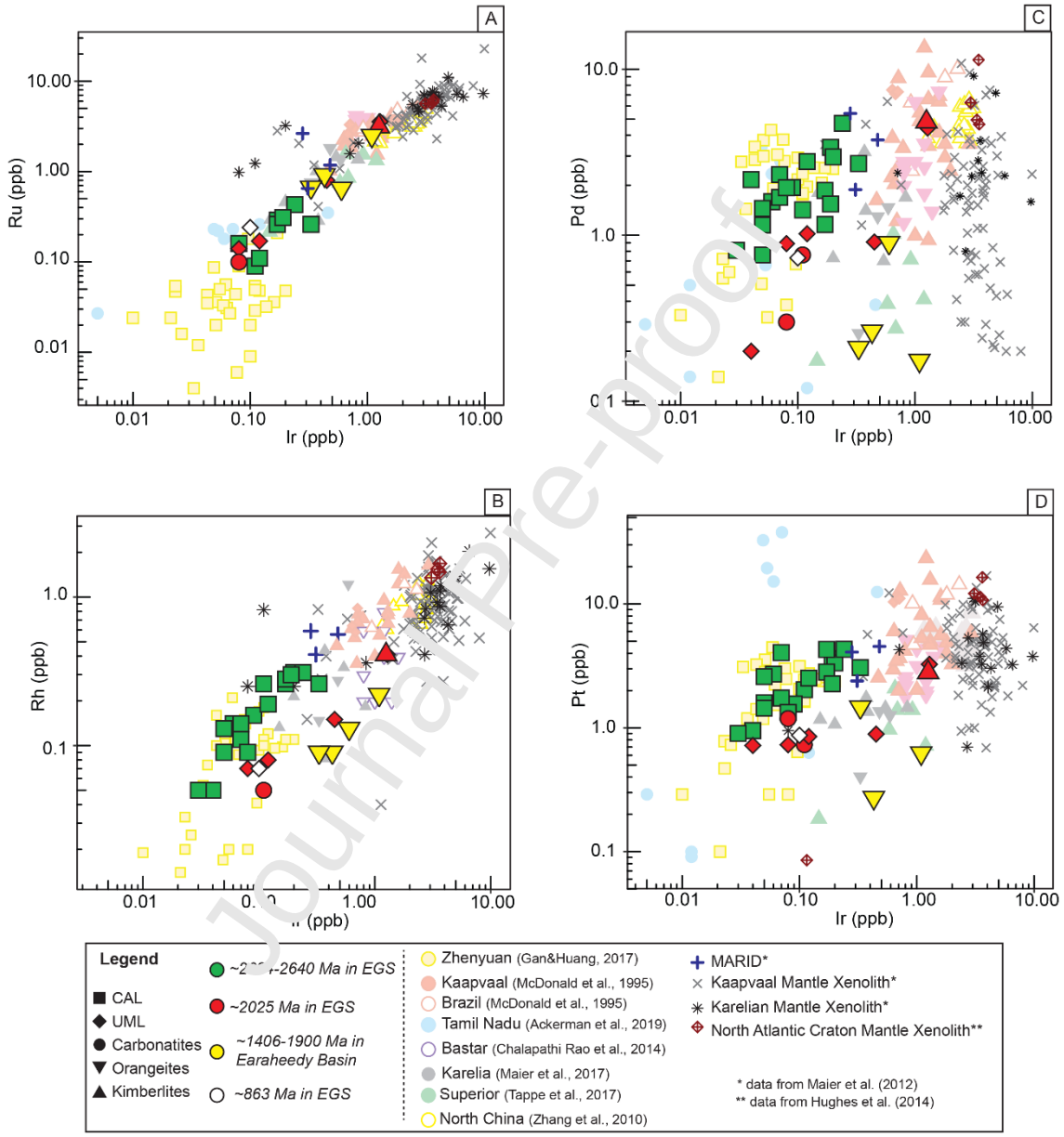

Fig. 5 Binary plots for PGE versus Ir contents for samples of CAL, UML, carbonatites, orangeites and kimberlites from the Yilgarn Craton and selected localities globally.

Table 1 Au and PGE concentrations in the examined examples from this study. Additional values for MgO, Ni, Cr and Cu are provided.

Sample	Age	Alteration Index*	Region	Au (ppb)	Ir	Pd	Pt	Rh	Ru	$(Pd/Ir)_N$	$(Pd/Pt)_N$	S (wt.%)	MgO* (wt.%)	Ni* (ppm)	Cr* (ppm)	Cu* (ppm)
Calc-alkaline lamprophyres (CAL) within the EGS																
128198	~2684-2640 Ma[1, 2]	I	Leonora	13.81	0.33	2.70	3.07	0.26	0.26	4.0	0.9	0.006	7.92	221.8	624	29.9
128181	~2684-2640 Ma[1, 2]	III	Leonora	5.30	0.09	1.94	1.56	0.16	<0.08	10.6	1.3	0.007	7.01	62.8	387	56.4
128186	~2684-2640 Ma[1, 2]	II	New Celebration	7.41	0.06	1.59	2.72	0.14	<0.08	13.1	0.6	0.472	7.04	122.4	425	111
128210	~2684-2640 Ma[1, 2]	I	New Celebration	6.61	0.05	1.45	2.59	0.13	<0.08	14.3	0.6	0.41	6.85	124.8	422	107
128200	~2684-2640 Ma[1, 2]	III	New Celebration	5.70	0.11	1.42	2.03	0.26	0.09	6.4	0.7	<0.003	9.56	264	727	13.2
128178	~2684-2640 Ma[1, 2]	II	Murrin	4.87	0.20	2.96	3.34	0.31	<0.08	7.3	0.9	0.024	7.63	78.8	366	83
128191	~2684-2640 Ma[1, 2]	I	Minerie	4.53	0.05	0.76	1.59	0.09	<0.08	7.5	0.5	0.005	4.18	58.3	245	40.3
128182	~2684-2640 Ma[1, 2]	I	Minerie	3.49	0.07	2.32	4.05	0.11	<0.08	16.3	0.6	0.008	7.02	116.4	366	87.8
128193	~2684-2640 Ma[1, 2]	I	Minerie	6.46	0.19	3.38	3.62	0.30	<0.08	8.8	1.0	0.012	9.18	127.7	705	67.8
128180	~2684-2640 Ma[1, 2]	II	Minerie	0.40	0.07	1.69	1.74	0.14	<0.[illegible]	11.9	1.0	0.011	4.87	45.9	193	57.1
JD3-1	~2684-2640 Ma[1, 2]	II	Jundee	2.44	0.24	4.72	4.31	0.31	0.43	[illegible].7	1.2	0.005	11.94	372.7	957	31.1
JD4-1	~2684-2640 Ma[1, 2]	III	Jundee	0.77	0.04	2.16	0.95	0.05	<0.08	26.6	2.4	0.253	5.95	145.3	197	53.6
JD1	~2684-2640 Ma[1, 2]	III	Jundee	0.51	0.12	2.78	2.52	0.19	[illegible]	11.4	1.2	0.018	10.28	288.1	707	23.5
JD3-2a	~2684-2640 Ma[1, 2]	III	Jundee	<0.4	0.08	1.93	1.33	[illegible].09	[illegible].16	11.9	1.6	0.017	9.44	346.3	516	1.8
Z36408	~2684-2640 Ma[1, 2]	II	Kambalda	2.50	0.17	1.86	4.30	[illegible].2	[illegible].29	5.4	0.5	<0.003	8.34	203.1	772	8.9
Z36413	~2684-2640 Ma[1, 2]	II	Kambalda	0.50	0.17	1.16	2.82	[illegible].28	0.26	3.4	0.4	0.003	9.05	228.9	858	9.4
Z36406	~2684-2640 Ma[1, 2]	I	Kambalda	0.40	0.19	1.54	[illegible].27	0.30	0.31	4.0	0.7	<0.003	9.58	246.5	929	10.6
Z27949	~2684-2640 Ma[1, 2]	II	Kambalda	1.20	0.05	1.15	[illegible].44	[illegible].09	<0.08	11.3	0.9	0.009	6.96	129.6	405	35
Z18500	~2684-2640 Ma[1, 2]	I	Kambalda	<0.4	0.03	0.81	[illegible].90	0.05	<0.08	13.3	1.0	<0.003	4.56	75.1	242	23.8
Ultramafic lamprophyres (UML) within the EGS																
Lara1	~2025 Ma[3]	II	Lara	1.00	0.1[illegible]	[illegible].92	0.85	0.08	0.17	4.2	1.3	0.256	13.51	282.7	276	104
128207	~2025 Ma[3]	II	Lara	0.90	0.0[illegible]	0.89	0.73	0.07	0.14	5.5	1.3	0.873	14.19	235.7	164	162
Melita1	~2025 Ma[3]	II	Melita	1.[illegible]0	[illegible].28	4.42	3.26	0.41	3.56	1.7	1.5	0.003	21.22	1613	2192	4.9
Melita3	~2025 Ma[3]	III	Melita	0.[illegible]	0.45	0.91	0.89	0.15	0.80	1.0	1.1	0.006	8.67	671.8	385	69.6
AKB-1	~2025 Ma[3]	II	Melrose Akbar	2.66	[illegible].04	0.20	0.72	<0.04	<0.08	2.5	0.3	0.005	13.56	95.1	115	21.6
AN01	~863 Ma[4]	I	Norseman	9.80	0.10	0.73	0.87	0.07	0.24	3.6	0.9	0.038	16.39	303.2	427	98.7
Carbonatites within the EGS																
MW2	~2025 Ma[3]	II	Mt. Weld	<0.4	0.11	0.76	0.73	0.05	<0.08	3.4	1.1	0.074	13.61	28	41	273
CH04-5	~2025 Ma[3]	I	Mt. Weld	<0.4	0.01	<0.12	<0.17	<0.04	<0.08	N/A	N/A	0.035	2.24	7.6	<3	21.3
CH04-3	~2025 Ma[3]	I	Mt. Weld	0.50	0.01	<0.12	<0.17	<0.04	<0.08	N/A	N/A	0.013	1.71	11.6	3	11.4
128211	~2025 Ma[3]	I	Mt. Weld	3.71	0.08	0.30	1.19	<0.04	0.10	1.8	0.3	0.045	10.22	152.2	215	167
Orangeites in the Earaheedy Basin																
BJ-5-5	~1406 Ma[5]	I	Bu[illegible]	<0.4	0.60	0.90	<0.17	0.13	0.65	0.7	N/A	0.016	16.62	458.6	566	50.2
BJ-5-1	~1406 Ma[5]	I	B[illegible]lljah	3.76	0.33	0.21	1.47	0.09	0.67	0.3	0.2	0.009	17.56	500	587	56.2
N#92-7	~1700-1900 Ma[6]	II	[illegible]abberu	<0.4	1.09	0.16	0.55	0.22	2.10	0.1	0.3	bdl	25.17	1221	1457	3.5
N#92-5	~1700-1900 Ma[6]	III	Nabberu	<0.4	0.43	0.24	0.24	0.09	0.77	0.3	1.1	0.006	25.43	530.5	559	<1.4
Kimberlites within the EGS																
Teutonic 1	~2025 Ma[3]	III	Teutonic Bore	<0.4	0.01	<0.12	<0.17	<0.04	<0.08	N/A	N/A	0.001	30.33	47.1	11	<1.4
Turkey2	~2025 Ma[3]	III	Turkey	<0.4	1.25	4.82	2.80	0.41	3.14	1.9	1.8	0.021	3.04	1555	883	82.2

Note: alteration index I = fresh; II = moderately altered; III = highly altered (see main text for details).
*data of CAL samples from Choi et al. (2020), and of UML, carbonatites, orangeites and kimberlites from Choi (2020)
Details about the alteration index are described in the main text.
[1] McNaughton et al. (2005), [2] Perring et al. (1989), [3] Graham et al. (2004), [4] Robey et al. (1989), [5] Choi (2020), and [6] Shee et al. (1999).

5. Discussion

In the following sections, we first assess the degree of contamination of the rocks examined in this study, which may have affected their platinum-group element and gold concentrations. On the basis of integrated petrographic, mineral chemistry and isotopic information, we show that whereas the

precious element concentrations in kimberlites may have been at least partially controlled by post-magmatic processes, results from the CAL and UML appear to reflect primary petrogenetic processes. Finally, we discuss how the exceptional gold fertility of the Eastern Goldfields Superterrane may be ultimately linked to its specific Late Archean geodynamic context.

5.1. Evaluation of post-magmatic processes on PGE-Au geochemistry

The calc-alkaline and alkaline ultramafic rocks from the Yilgarn Craton and its northern margin have undergone various degrees of post-magmatic modification. Recent studies of these rocks reported three alteration indices based on detailed petrographic evidence (Choi, 2020; Choi et al., 2020):

a) alteration index I is applied to the least altered samples, characterised by fresh phenocrysts and minor presence of alteration phases (e.g., minor albitisation in the groundmass of CAL);

b) alteration index II is for samples with preservation of 40-70% of the primary mineral assemblages; and

c) alteration index III applies to extremely sheared and/or altered samples, where primary mineral assemblages and igneous textures are poorly preserved (less than 40 %), or not preserved at all.

The Late Archean CAL from the Eastern Goldfields Superterrane experienced low-temperature greenschist facies metamorphism (Perring et al., 1989), reflected in the alteration of calcic amphibole to actinolite, biotite chloritisation and groundmass albitisation. Carbonation and chloritisation are prominent in three samples from Jundee, whereas samples from New Celebration (128200) and Leonora (128181) exhibit severe carbonation, chloritisation and albitisation (alteration index III). The Paleoproterozoic UML from the Eastern Goldfields Superterrane (except Norseman) have partially altered phlogopite phenocrysts and olivine phenocrysts that are completely pseudomorphed by chlorite, serpentine or carbonate (alteration index II; Table 1). The Melita 3 sample represents an exception as it is heavily weathered (alteration index III). The EGS kimberlites display pervasive

silicification that, combined with extensive serpentinisation, makes the original textures unrecognisable (alteration index III). Similarly, the Nabberu orangeites have sheared textures with abundant chlorite, serpentine and carbonate, which reflect post-magmatic deformation probably associated with extensive influxes of crustal fluids (alteration index III). Conversely, the orangeites from Bulljah and carbonatites from Mt. Weld are significantly less weathered (alteration index I). Evidence of post-magmatic processes is recorded in most of the calc-alkaline and alkaline ultramafic samples investigated in this study. The question is to what extent the various degrees of post-magmatic modification may have affected the PGE and Au contents of the investigated samples.

The orangeites from Nabberu display unusual negative trends in the PGE patterns compared to the trends of orangeites or kimberlites globally (Fig. 2D), which could reflect preferential mobilisation of Pd and Pt during hydrothermal alteration (e.g., Ballhaus and Stumpfl, 1986; Barnes and Liu, 2012; Guice et al., 2019; Le Vaillant et al., 2016). The kimberlite from Teutonic Bore contains PGE contents that are mostly below detection limit (Table 1). Whereas this signature could be explained by PGE and Au removal during sulfide leaching, this interpretation remains at odds with the typically kimberlitic primitive mantle-normalised PGE pattern of the equally altered Turkey Well kimberlite sample (Fig. 2E). Therefore, data from the Turkey Well kimberlite suggest that despite petrographic evidence for deformation and post-magmatic alteration, modification of PGE concentrations - and especially of the less mobile Ir-group PGEs (IPGE; Ir, and Ru) - may still be limited in some highly altered samples.

The CAL and UML samples investigated in this study display internally coherent primitive mantle-normalised PGE patterns with a positive slope and flat outline, respectively (Fig. 2A, B), reflecting limited PGE disturbance during alteration despite various degrees of secondary post-magmatic effect. The orangeites from Bulljah display flat PGE patterns that are similar to those from kimberlites and orangeites globally (Fig. 2D). The Bulljah samples contain lower PGE contents than orangeites from the Bastar Craton (Chalapathi Rao et al., 2014). However, these lower contents are also observed in orangeites from the Karelian Craton (Maier et al., 2017). Hence, although the PGE concentrations in few samples (e.g., Teutonic Bore kimberlite, Nabberu orangeites) were affected by

post-emplacement modification, data from all CAL and UML samples as well as from the Bulljah orangeite indicate that the effect of post-magmatic processes on PGE mobilisation may be limited.

Taylor et al. (1994) suggested that anomalously enriched Au signatures in some CAL from the Eastern Goldfields Superterrane could result from the influx of Au-bearing hydrothermal fluids during regional greenschist-facies metamorphism rather than being primary features of these rocks. These authors suggested a correlation between high Au contents from 12 ppb to ~3000 ppb and degree of carbonation, which was reflected by higher whole-rock CO_2 contents (up to 7.6 wt.%) than the average content in global CAL (~0.5 wt.%; Rock, 1991). The higher Au contents reported by Taylor et al. (1994) may result from the limited accuracy of the analytical techniques, as discussed above. Despite various degrees of post-magmatic alteration, Au contents of CAL samples with alteration index III range from 0.5 ppb to 5.7 ppb, whereas CAL samples with alteration index I contain 0.4 ppb to 13.8 ppb Au; hence, there is no correlation between Au content and the degree of alteration. Even though the CO_2 contents of the CAL samples (alteration index I and II) range up to ~4.0 wt.% (Choi et al., 2020), no correlation between whole rock CO_2 and Au concentrations can be identified in the CAL samples from this study (Fig. 6).

In order to fully evaluate the significance of the PGE-Au dataset to constrain primary petrogenetic processes, it is important to assess the extent of contamination due to entrainment of lithic fragments as well as crustal and mantle xenoliths. Choi (2020) and Choi et al. (2020) previously showed that the majority of CAL and alkaline ultramafic samples employed in this study experienced negligible amounts of crustal contamination based on trace element and radiogenic isotope systematics. In addition, although few clinopyroxene macrocrysts in the Lara UML were reported as xenocrysts, no crustal or mantle xenoliths were observed in the examined samples (Choi, 2020). Furthermore, any correlation of PGE, Au and S contents with indicators of crustal assimilation (e.g., Th/La) is not observed (Supplementary Figure 1). Kimberlites are probably the only exception because these rocks commonly contain abundant mantle fragments (e.g., Giuliani, 2018; Mitchell et al., 2019); however, the two kimberlite samples from this study are so altered that the contribution from any entrained material from the lithospheric mantle could not be assessed.

In summary, even if deformation and post-magmatic alteration may locally affect the primary PGE-Au signatures, significant mobilisation is only observed in one of the EGS kimberlites and in the Nabberu orangeites (Fig. 1). Conversely, the newly generated data for UML, carbonatites and CAL show minimal effects of post-magmatic modification beyond potential dilution due to local addition of hydrothermal components. Therefore, the PGE and Au data of the CAL, UML and carbonatites documented in this study can be used as reliable indicators of the PGE-Au geochemical nature of the mantle sources underlying the Yilgarn Craton at the time of emplacement of these magmas.

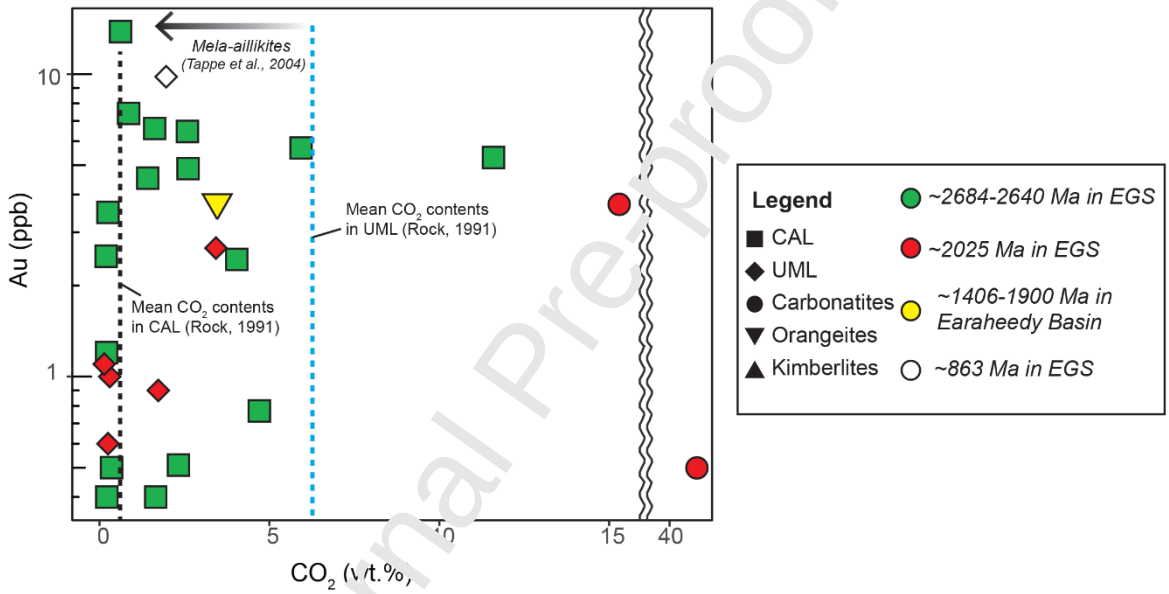

Fig. 6 Whole-rock CO_2 (wt.%) versus Au (ppb) diagram for the calc-alkaline and alkaline ultramafic rocks investigated in this study.

5.2. PGE signatures in kimberlites and orangeites

Caution is needed in the interpretation of these data for the lines of argument that were discussed in the previous section. However, PGE-Au results from some of these rocks (e.g., the fresh orangeites from Bulljah) are still valuable to unveil some key processes pertaining to their petrogenesis. Orangeite samples from Bulljah, in the Earaheedy Basin have unfractionated PGE patterns and low $(Pd/Ir)_N$ ratios (up to ~1), which are similar to the PGE signature of kimberlites and orangeites globally (Maier et al., 2017; McDonald et al., 1995). The orangeites from Bulljah and elsewhere

probably derived from low-degree partial melting of lithospheric mantle sources that experienced ancient metasomatic enrichment, reflected in their highly elevated incompatible trace elements and enriched Sr-Nd-Hf isotope compositions (Choi, 2020; Giuliani et al., 2015; Nowell et al., 2004). Also, the metasomatised SCLM is considered to be relatively oxidised (e.g., Yaxley et al., 2017), which would facilitate the breakdown of sulfides and metal alloys and transfer for their metal budget into silicate melts (Tassara et al., 2020). Taken together, the observed flat PGE patterns with moderately high IPGE values may reflect the contribution of IPGE-rich and relatively oxidised peridotitic material from SCLM.

The Turkey Well kimberlite displays a flat PGE pattern, which is similar to the one that characterises kimberlites globally (Fig. 2E), including very fresh samples from Renard (Superior Craton; Tappe et al., 2017). The flat PGE patterns of kimberlites elsewhere are generally attributed to a combination of fractionation between IPGE and PPGE with relative PPGE enrichment during partial melting, combined with entrainment of IPGE-rich xenocrystic material during ascent (McDonald et al., 1995; Maier et al., 2017). A similar model could be applied to the Turkey Well sample examined here. However, due to the insufficient number of both orangeite and kimberlite samples, as well as to the elevated degree of post-magmatic alteration, further work will be required to put forward a conclusive hypothesis.

5.3. Insights into the petrogenesis of ultramafic lamprophyres and carbonatites from PGE-Au geochemistry

The UML and carbonatites from the EGS have been suggested to have a genetic link based on overlapping Nd-Hf-Sr-Pb-Os-C isotope compositions (Choi, 2020; Graham et al., 2004). Enriched incompatible trace elements and circa-chondritic radiogenic isotope compositions of these rocks suggest generation by low-degree partial melting of the convective mantle with negligible contribution from enriched lithospheric mantle material (Choi, 2020). The UML and carbonatites analysed in this study have relatively unfractionated PGE patterns with low $(Pd/Ir)_N$ ratios (up to ~6). These values are also observed in global kimberlite occurrences and are considered to reflect low-

degree partial melting of their mantle sources [$(Pd/Ir)_N$ = up to ~8; Maier and Barnes, 2004; McDonald et al., 1995 and references therein].

Mantle sulfides are normally considered to be exhausted during moderate to large degrees of mantle melting (> 15-25 %; Barnes et al., 1985; Mungall and Brenan, 2014), assuming an average concentration of 250 ppm S in the mantle (McDonough and Sun, 1995). At lower degrees of partial melting (5-15 %), sulfides would melt incongruently, thus preferentially releasing highly chalcophile elements such as Pt, Pd, Au and Cu in the resulting silicate melt (Ballhaus et al., 2006). This process would result in a variably fractionated PGE pattern (cf. Holwell et al., 2019). At even lower degrees of partial melting (<5 %), mantle sulfides may be largely retained in the source without significant fractionation between IPGE and PPGE. Hence, very low-degree melts would have low PGE concentrations combined with unfractionated PGE patterns resembling those of their mantle sources. This scenario may apply to the petrogenesis of the UML and carbonatites in the Yilgarn Craton. However, it is acknowledged that this interpretation may be speculative and may require further testing in the future. It is also understood that the extremely low values were only detected because of the highly sensitive analytical procedure that was adopted here to measure them. It is likely that such low concentrations would be below detection limit of most commercial analytical techniques.

Alternatively, rather than reflection of extremely low degrees of partial melting of the mantle, it may be argued that the low PGE contents in the UML and carbonatites may reflect sulfide saturation during magma ascent. Experiments have shown that the solubility of sulfur decreases exponentially with increasing pressure, and that melts become increasingly sulfide-undersaturated during ascent, unless significant melt fractionation and/or assimilation of S-rich sediments occur (Mavrogenes and O'Neill, 1999). Our data indicate that whole-rock S contents in most UML and carbonatites from the EGS are low, i.e. <0.1 wt.%; only few samples contain higher contents, which are manifested as rare occurrences of secondary sulfides (Table 1). Furthermore, assimilation of S-rich contaminants can be excluded based on the geochemical features of these magmas (i.e. juvenile radiogenic isotope compositions; Choi, 2020). Therefore, combined evidence suggests that the ubiquitous PGE depletion in the UML and carbonatites investigated in this study was not caused by sulfide segregation from the

magma. Given the current constraints, sulfide retention in the mantle is deemed to be the key controlling factor.

Elevated Au contents are observed in some UML samples from the Yilgarn Craton. This observation is potentially consistent with studies reporting elevated Au contents in kimberlites from the Kaapvaal (McDonald et al., 1995) and North China cratons (Zhang et al., 2010), as well as mantle xenoliths from the Kaapvaal, Karelian and North Atlantic cratons (Hughes et al., 2014; Maier et al., 2012; Fig. 7A). If kimberlites and carbonate-rich UML are derived from common convective mantle sources through time (Choi, 2020; Woodhead et al., 2019), these results may suggest a widespread and long-lived enrichment in Au in the convective mantle. Alternatively, Au enrichment might be due to the physical entrainment and/or assimilation of locally Au-rich lithospheric material, as indicated by Au enrichment in some mantle xenoliths. In particular, a redox gradient during ascent of asthenospheric-derived mantle melts reacting with lithospheric mantle wall-rock may facilitate the breakdown of sulfides or dissolution of Au-bearing alloys and release of Au (Tassara et al., 2020). A more comprehensive assessment of Au compositions in alkaline ultramafic magmas and mantle xenoliths worldwide will be required to test these hypotheses.

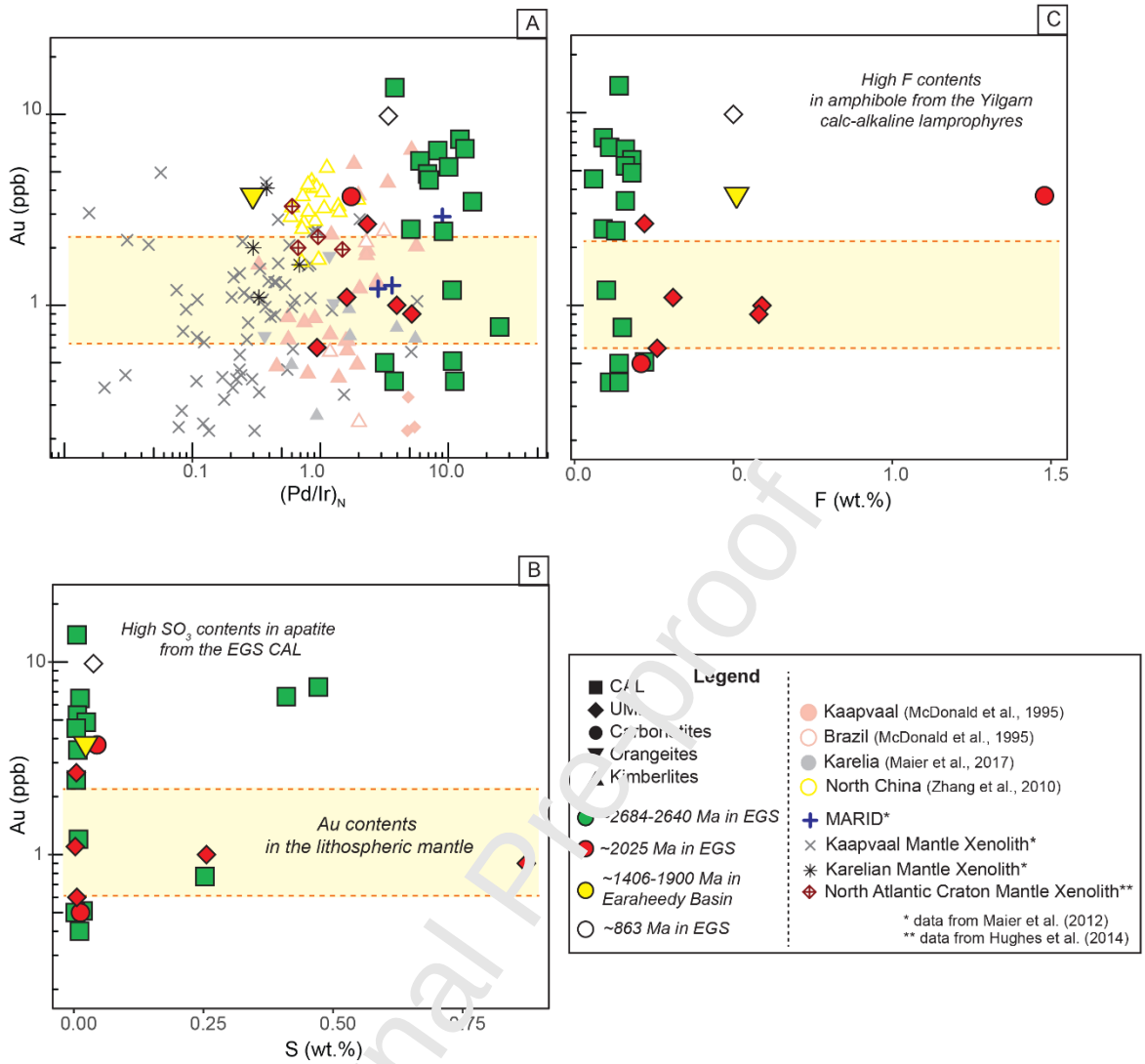

Fig. 7 Au (ppb) versus (A) $(Pd/Ir)_N$, (B) S (wt. %) and (C) F concentrations (wt. %) in the examined samples. The compositional field (yellow) of Au contents in the lithospheric mantle is from Saunders et al. (2018).

5.4. Controls and nature of PGE distribution in calc-alkaline lamprophyres (CAL)

The CAL display distinctive PGE signatures including 1) low IPGE contents, 2) fractionated PGE patterns [$(Pd/Ir)_N$ up to ~50], 3) $(Pd/Pt)_N$ of ~1, and 4) elevated Au contents. These features may be inherited from the source and/or acquired upon ascent and emplacement. First, we consider whether the PGE signature of the CAL could be due to sulfide-supersaturation following crustal contamination. Similarly to the UML above, whole-rock S concentrations in most of the CAL are <0.1 wt.%; only few samples contain higher S contents, which are manifested as rare occurrences of

secondary sulfides (Table 1). Choi et al. (2020) reported that few occurrences of secondary pyrite were observed in several CAL samples in this study (JD4-1, JD1, Z27949, Z18500 and 128210). Au concentrations in these secondary pyrite-bearing samples are from <0.4 ppb (below detection limit) to 6.61 ppb, which are within the range of other CAL samples in this study. This demonstrates that there is no correlation between the abundance of secondary pyrite and bulk-sample Au concentrations. Therefore, even if it is thought that the primary melts that originated CAL elsewhere may have been sulfide-saturated at the source (Barnes et al., 1985; Keays, 1982; Maier and Barnes, 2004), the inverse relationship between sulfur solubility and pressure would have prevented sulfide segregation upon ascent. As a result and based on the lack of correlation between PGE or Au concentrations and extent of alteration (see Section 5.1), we suggest that the PGE-Au signature of the CAL investigated in this study probably reflects the source signatures.

Fractionated PGE patterns are the most distinctive features of the CAL compared to the other rocks examined in this study. These patterns are consistent with the inferred low-degree partial melting of the source and associated incongruent melting of mantle sulfides with potential contribution from platinum-group minerals and metal alloys in the source (cf. Holwell et al., 2019). Low-degree melting would preferentially liberate incompatible PPGE and Au over the more refractory IPGE. A positive correlation between Ir and MgO concentrations in the examined CAL is observed (Fig. 3A) indicates that bulk-sample PGE concentrations are affected by variable extent of partial melting. However, the similar Pt and Pd concentrations (0.8-4.7 ppb; 1.0-4.3 ppb, respectively) as well as the variable and significantly elevated Au contents (up to 13.8 ppb) in these magmas cannot be explained by the degree of partial melting alone because i) Pd would fractionate from Pt, and ii) Au contents would be lower than observed. We propose that the observed enrichments in Pt and Au may reflect the superimposed effects of slab-related fluid fluxing, which metasomatised the lithospheric mantle source of the CAL (Choi et al., 2020).

Similar $(Pd/Pt)_N$ ratios close to unity observed in these CAL are also reported in mantle xenoliths in arc settings (Kepezhinskas and Defant, 2001). These authors suggested that the mantle wedge above subduction zones may be anomalously enriched in Pt, leading to the formation of Pt-enriched primary melts in arc settings. This inference is supported by the depleted PPGE signatures relative to

IPGE in subducted mafic oceanic crust (i.e. eclogites), suggesting that Pt and Pd may be transferred to the mantle wedge by slab-derived fluids (Dale et al., 2009). Peridotite mantle xenoliths enriched in Pt are also reported in the North Atlantic Craton, which is inferred to have been previously enriched by a subduction event (Hughes et al., 2017). Accordingly, the anomalously elevated Pt abundance in the CAL could be due to selective Pt enrichment relative to Pd in the subduction-related fluids that metasomatised the CAL source (Brenan et al., 2016). Although Pd, Pt and Au concentrations are not correlated to slab-derived components (e.g., LILE) in the CAL from the EGS, the Pt enrichment could indicate a significant role of subduction-related fluids in PGE-Au geochemistry of the studied samples.

The observed elevated Au signatures in the CAL (Fig. 7A) were also reported in other calc-alkaline and alkaline magmas globally (Holwell et al., 2019; Zhang et al., 2010), as well as in mantle xenoliths and basalts affected by subduction-related processes (Tassara et al., 2017; Wang et al., 2020). Several studies on these subduction-related calc-alkaline magmas and mantle xenoliths suggested that subduction-related metasomatism may introduce volatile elements from the subducted slab into the lithospheric mantle, forming gold- and volatile-rich assemblages in the metasomatised mantle (Holwell et al., 2019). Wang et al. (2020) proposed that the volatile components of SCLM, which would have been added during metasomatism, facilitated the release of Au during subsequent partial melting of that metasomatised mantle. A similar metasomatic process might have enriched the lithospheric mantle source of CAL in the EGS thus stimulating Au release into CAL magmas during mantle melting.

Although no correlation of whole-rock F and S with Au concentrations in the CAL is observed (Fig. 7B, C), the CAL display the highest Au contents among all samples investigated in this study; these rocks also contain ubiquitous apatite with anomalously high S concentrations (SO_3 up to 1.0 wt.%; Choi et al., 2020), which are much higher than typical contents in apatite from other silicate and carbonatite magmas worldwide (average SO_3 ~0.2 wt.%; Belousova et al., 2002; Chakhmouradian et al., 2017; Webster and Piccoli, 2015). In addition, CAL sample 128198 from Leonora (Fig. 1) shows the highest Au content of 13.8 ppb and contains the most F-rich amphibole phenocrysts (up to ~0.6 wt.% F; Choi et al., 2020). These values may hint to a correlation between elevated volatile (S, P, F)

contents in magmatic minerals and high whole-rock Au concentrations (Fig. 7B, C). This observation may support a model whereby slab-derived fluids introduced Au and volatiles in the SCLM beneath the Eastern Goldfields (Fig. 8; Stage I), and volatile enrichment promoted the release of Au into the CAL magmas (Fig. 8; Stage III).

In summary, this correlation may support the hypothesis that slab-derived fluids transport volatiles from a subducting slab into the lithospheric mantle, as suggested by Tassara et al. (2017) and Holwell et al. (2019). Furthermore, volatile enrichment of the lithospheric mantle may promote transfer of Au into silicate magmas during partial melting (Wang et al., 2020). Our proposed model illustrated in Figure 8 and based on Choi et al. (2020), suggests the following petrogenetic processes: Fluid exsolution from the subducted slab (Stage I) triggered flush melting of the metasomatised lithospheric mantle (Stage II) thus inducing incongruent melting of mantle sulfides with potential contributions from PPGE and/or Au-bearing metal alloys and facilitating the release of Au in primary CAL melts (Stage III). Finally, the parental magmas of the CAL ascend through the SCLM and are emplaced into the crust (Stage IV). It is proposed that these sequential processes imparted the CAL magmas with a gold-enriched metallogenic signature (Fig. 8).

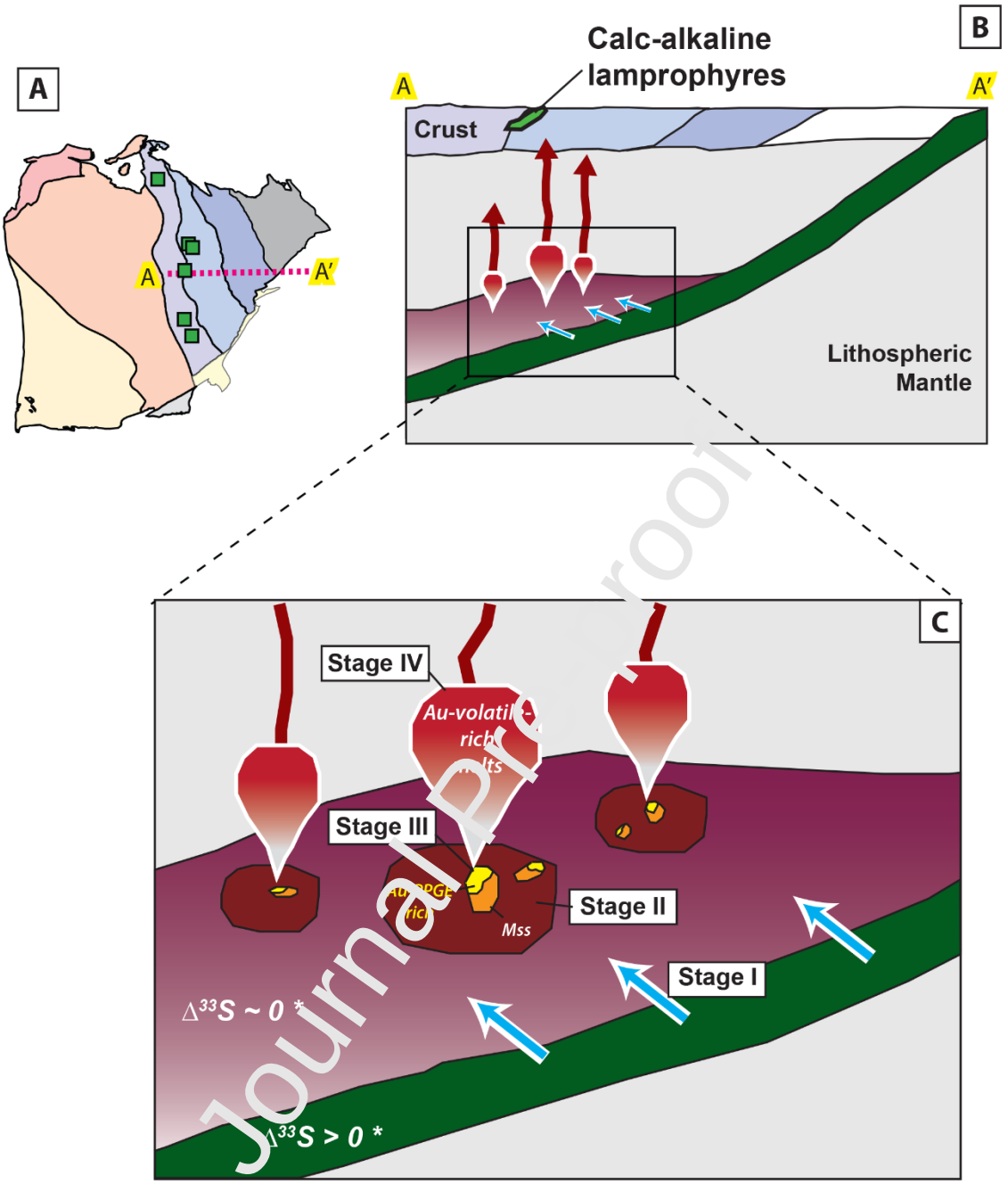

Fig. 8 Cartoon illustrating the proposed model for the metallogenic endowment of the Eastern Goldfields Superterrane, associated with the petrogenesis of Late Archean subduction-related CAL. (A) Location of the CAL collected in this study. (B) Infiltration of the lithospheric mantle by subduction-related fluids, which trigger flush melting and the genesis of the Late Archean CAL. (C) Enlarged view of B, with overview of the four-stage genetic process of CAL and related metallogenic endowment. Stage I: fluids enriched in H_2O, CO_2, P, F and S are generated by break-down of amphibole and sulfide-bearing sediments in the subducted slab ($\Delta^{33}S > 0$; Laflamme et al., 2018);

Stage II: flush melting of the metasomatised lithospheric mantle triggers low-degree partial melting; Stage III: this process induces incongruent melting of mantle sulfides (Mungall and Brenan, 2014), which are known to have $\Delta^{33}S \sim 0$, with potential contribution from Au-bearing alloys. Incongruent melting of sulfides during low-degree partial melting of the mantle would preferentially leave behind some of the Ni–Os–Ir–Ru-rich monosulfide solid solid solution (mss; orange domains), but liberate the Cu-sulfide and Au–Pt–Pd–Te phases (yellow domains), which have lower melting temperatures; Stage IV: this process primes ascending CAL magmas with their precious element budget. $\Delta^{33}S$ data from LaFlamme et al. (2018).

5.5. First-order control on Au endowment in the Eastern Goldfields Superterrane

The Eastern Goldfields Superterrane is one of the most metal-endowed geological regions in the world, and currently a major contributor to the economy of Western Australia as the premier producer for gold (e.g., Aitken et al., 2018; Blewett et al., 2010b; Groves et al., 1995). The timing of gold mineralisation in the Eastern Goldfields Superterrane has been constrained between ca. 2650 and 2620 Ma (e.g., Cassidy et al., 2002; Czarnota et al., 2010; Kent et al., 1996; Mole et al., 2013). This temporal window broadly overlaps with the timing of emplacement of the CAL magmas at 2684-2640 Ma (McNaughton et al., 2005; Perring et al., 1989; Smithies et al., 2018a; Vielreicher et al., 2015). We suggest that this synchronicity is at the heart of the exceptional gold endowment of the EGS: at a time when this crustal block was experiencing significant orogenic events, its underlying lithosphere was being literally pervaded by volatiles, which promoted flush melting and the genesis of Au-rich hydrous melts. These melts were channelised and concentrated along different types of structural pathways (e.g., Cassidy et al., 2006; Groves et al., 1995).

It is proposed that this process occurred almost coevally at the scale of the EGS, based on the exceptional homogeneity of the radiogenic isotope signature of the CAL (Choi et al., 2020) and the uniform multiple sulfur isotope signature of orogenic gold deposits in the EGS, which shows a relatively constant $\Delta^{33}S$ signature of -1.18 ‰ to + 2.04 ‰ (Selvaraja et al., 2017a). This very slightly positive signature is broadly consistent with mixing and homogenisation of a mantle-dominated sulfur

reservoir with crustal sedimentary sulfur that may have been subducted and recycled (LaFlamme et al., 2018; Selvaraja et al., 2017b). In the EGS, the exceptional gold endowment of the Kalgoorlie Terrane in relation to other domains (Blewett et al., 2010a, 2010b; Cassidy et al., 2002; Mole et al., 2013) may be due to its relatively "stable" geodynamic framework, whereby it developed at the edge of a long-lived stable buoyant craton (the Youanmi Terrane of Mole et al., 2019). This setting provided the Kalgoorlie Terrane with the unique opportunity to be fluxed over a temporal window of at least 40 million years. Therefore, the Late Archean subduction-related metasomatic event that affected the lithospheric mantle of the Eastern Goldfields Superterrane may have provided a first-order control on its exceptional gold endowment.

6. Conclusions

This study presents a comprehensive platinum-group element and gold dataset of Late Archean calc-alkaline and Proterozoic alkaline and CO_2-rich mafic/ultramafic magmas from the Yilgarn Craton and its northern margin. The investigated samples show relatively low PGE contents, locally elevated Au contents, and a diverse range of PGE patterns, which are consistent with petrogenetic processes occurring in different geodynamic settings. Paleo- to Neoproterozoic UML and carbonatites from the convective mantle show PGE depletion and unfractionated patterns, with anomalous Au enrichment in few samples. The PGE signatures can be explained by sulfide retention in the source following extremely low degree partial melting of a convective mantle source. Although this hypothesis is conjectural due to the relatively small number of samples analysed in this study, the new results on gold contents in alkaline ultramafic magmas from the Yilgarn Craton may indicate the presence of Au-enriched domains in the mantle.

Subduction-related CAL in the Late Archean exhibit strongly fractionated PGE patterns, $(Pd/Pt)_N$ = ~1, and marked Au enrichment. The fractionated PGE patterns are attributed to low-degree partial melting of metasomatised mantle sources combined with incongruent melting of the mantle sulfides and potential contribution from PPGE- and Au-bearing alloys, which would preferentially contribute PPGE and Au over IPGE. Similar Pt and Pd contents combined with elevated Au concentrations and enrichments in volatile elements (S, F, H_2O) are consistent with CAL generation by flush melting of

the SCLM by slab-derived fluids. It is proposed that the volatile fluxing associated with a subduction-related process may have ultimately been the key factor that controlled the exceptional metallogenic fertility of the Eastern Goldfields Superterrane.

Acknowledgements

This work was financially supported by the Australian Government Research Training Program Scholarship, the Australian Research Council through the Centre of Excellence for Core to Crust Fluid Systems (CE1100001017), as well as the Minerals Research Institute of Western Australia. The authors thank Mark Mitchell (DeBeers) and Northern Star Resources for the donation of samples used in this study. This is contribution no. 1516 from the ARC Centre of Excellence for Core to Fluid Systems (http://www.ccfs.mq.edu.au). This is part of the PhD thesis of EC, who acknowledges the support of the University of Western Australia through a RTS scholarship. Detailed reviews by Sonja Aulbach and two anonymous reviewers improved the final manuscript.

References

Aitken, A., Occhipinti, S., Lindsay, M., Joly, A., Howard, H., Johnson, S., Hollis, J., Spaggiari, C., Tyler, I., McCuaig, T., 2018. The tectonics and mineral systems of Proterozoic Western Australia: Relationships with supercontinents and global secular change. Geoscience Frontiers 9, 295-316.

Ballhaus, C., Bockrath, C., Wohlgemuth-Ueberwasser, C., Laurenz, V., Berndt, J., 2006. Fractionation of the noble metals by physical processes. Contributions to Mineralogy and Petrology 152, 667-684.

Ballhaus, C.G., Stumpfl, E.F., 1986. Sulfide and platinum mineralization in the Merensky Reef: evidence from hydrous silicates and fluid inclusions. Contributions to Mineralogy and Petrology 94, 193-204.

Barley, M., Brown, S., Cas, R., Cassidy, K., Champion, D., Gardoll, S., Krapez, B., 2003. An integrated geological and metallogenic framework for the eastern Yilgarn Craton: developing geodynamic models of highly mineralised Archaean granite–greenstone terranes. AMIRA Project P 624.

Barley, M., Brown, S., Krapez, B., Cas, R., 2002. Tectonostratigraphic analysis of the eastern Yilgarn craton: An improved geological framework for exploration in Archaean terranes. AMIRA Project P437A, Final Report.

Barnes, S.-J., Naldrett, A., Gorton, M., 1985. The origin of the fractionation of platinum-group elements in terrestrial magmas. Chemical Geology 53, 303-323.

Barnes, S.J., Fiorentini, M.L., 2008. Iridium, ruthenium and rhodium in komatiites: evidence for iridium alloy saturation. Chemical Geology 257, 44-58.

Barnes, S.J., Fiorentini, M.L., 2012. Komatiite magmas and sulfide nickel deposits: A comparison of variably endowed Archean terranes. Economic Geology 107, 755-780.

Barnes, S.J., Liu, W., 2012. Pt and Pd mobility in hydrothermal fluids: evidence from komatiites and from thermodynamic modelling. Ore Geology Reviews 44, 49-58.

Barnes, S.J., Van Kranendonk, M.J., 2014. Archean andesites in the east Yilgarn craton, Australia: Products of plume-crust interaction? Lithosphere 6, 80-92.

Becker, M., Le Roex, A.P., 2006. Geochemistry of South African on-and off-craton, Group I and Group II kimberlites: petrogenesis and source region evolution. Journal of Petrology 47, 673-703.

Belousova, E., Griffin, W., O'Reilly, S.Y., Fisher, N., 2002. Apatite as an indicator mineral for mineral exploration: trace-element compositions and their relationship to host rock type. Journal of Geochemical Exploration 76, 45-69.

Blewett, R., Czarnota, K., Henson, P., 2010a. Structural-event framework for the eastern Yilgarn Craton, Western Australia, and its implications for orogenic gold. Precambrian Research 183, 203-229.

Blewett, R.S., Henson, P.A., Roy, I.G., Champion, D.C., Cassidy, K.F., 2010b. Scale-integrated architecture of a world-class gold mineral system: the Archaean eastern Yilgarn Craton, Western Australia. Precambrian Research 183, 230-250.

Brenan, J.M., Bennett, N.R., Zajacz, Z., 2016. Experimental results on fractionation of the highly siderophile elements (HSE) at variable pressures and temperatures during planetary and magmatic differentiation. Reviews in Mineralogy and Geochemistry 81, 1-87.

Brey, G.P., Bulatov, V.K., Girnis, A.V., Lahaye, Y., 2008. Experimental melting of carbonated peridotite at 6–10 GPa. Journal of Petrology 49, 797-821.

Cassidy, K.f., Champion, D.C., Krapez, B., Barley, M.E., Brown, S.J.A., Bleweet, R.S., Groenewald, P.B., Tyler, I.M., 2006. A revised geological framework for the Yilgarn Craton, Western Australia. Geological Survey of Western Australia, Record 2006/8.

Cassidy, K.F., Champion, D.C., McNaughton, N., Fletcher, I., Whitaker, A.J., Bastrakova, I.V., Budd, A.R., 2002. Characterisation and Metallogenic Significance of Archaean Granitoids of the Yilgarn Craton, Western Australia: Results of Research Carried Out as MERIWA Project No. M281 at the Key Centre for Strategic Mineral Deposits, the University of Western Australia and Australian Geological Survey Organisation. Minerals and Energy Research Institute of Western Australia.

Chakhmouradian, A.R., Reguir, E.P., Zaitsev, A.N., Couëslan, C., Xu, C., Kynický, J., Mumin, A.H., Yang, P., 2017. Apatite in carbonatitic rocks: Compositional variation, zoning, element partitioning and petrogenetic significance. Lithos 274, 188-213.

Chalapathi Rao, N., Lehmann, B., Balaram, V., 2014. Platinum-group element (PGE) geochemistry of Deccan orangeites, Bastar craton, central India: implication for a non-terrestrial origin for iridium enrichment at the K–Pg boundary. Journal of Asian Earth Sciences 84, 24-33.

Chalapathi Rao, N., Lehmann, B., Mainkar, D., Belyatsky, B., 2011. Petrogenesis of the end-Cretaceous diamondiferous Behradih orangeite pipe: implication for mantle plume–lithosphere interaction in the Bastar craton, Central India. Contributions to Mineralogy and Petrology 161, 721-742.

Choi, E., 2020. Alkaline magmatism as a probe into the evolution of the lithospheric mantle in the Yilgarn Craton, Western Australia. University of Western Australia.

Choi, E., Fiorentini, M.L., Giuliani, A., Foley, F., Stephen, Maas, R., Taylor, W.R., 2020. Subduction-related petrogenesis of Late Archean calc-alkaline lamprophyres in the Yilgarn Craton (Western Australia) Precambrian Research 338, 105550.

Choi, E., Fiorentini, M.L., Giuliani, A., Foley, S.F., Maas, R., Graham, S., in revision. Petrogenesis of Proterozoic alkaline ultramafic rocks in the Yilgarn Craton, Western Australia.

Clark, D., Hensen, B., Kinny, P., 2000. Geochronological constraints for a two-stage history of the Albany–Fraser Orogen, Western Australia. Precambrian Research 102, 155-183.

Coe, N., Le Roex, A., Gurney, J., Pearson, D.G., Nowell, G., 2008. Petrogenesis of the Swartruggens and Star Group II kimberlite dyke swarms, South Africa: constraints from whole rock geochemistry. Contributions to Mineralogy and Petrology 156, 627.

Compston, W., Williams, I., Pidgeon, R., Gresham, J., 1985. The age of the Kambalda sodic granodiorite. Australian National University, Research School of Earth Sciences, Annual Report 1985, 95-96.

Currie, K.L., Williams, P.R., 1993. An Archean calc-alkaline lamprophyre suite, northeastern Yilgarn Block, western Australia. Lithos 31, 33-50.

Czarnota, K., Champion, D., Goscombe, B., Blewett, R., Cassidy, K., Henson, P., Groenewald, P., 2010. Geodynamics of the eastern Yilgarn Craton. Precambrian Research 183, 175-202.

Dale, C., Burton, K., Pearson, D., Gannoun, A., Alard, O., Argles, T., Parkinson, I., 2009. Highly siderophile element behaviour accompanying subduction of oceanic crust: whole rock and mineral-scale insights from a high-pressure terrain. Geochimica et Cosmochimica Acta 73, 1394-1416.

Dalton, H., Giuliani, A., O'Brien, H., Phillips, D., Hergt, J., Maas, R., 2020. Petrogenesis of a hybrid cluster of evolved kimberlites and ultramafic lamprophyres in the Kuusamo area, Finland. Journal of Petrology.

Dalton, J.A., Presnall, D.C., 1998. The continuum of primary carbonatitic–kimberlitic melt compositions in equilibrium with lherzolite: data from the system CaO–MgO–Al2O3–SiO2–CO2 at 6 GPa. Journal of Petrology 39, 1953-1964.

Dasgupta, R., Hirschmann, M.M., McDonough, W.F., Spiegelman, M., Withers, A.C., 2009. Trace element partitioning between garnet lherzolite and carbonatite at 6.6 and 8.6 GPa with applications to the geochemistry of the mantle and of mantle-derived melts. Chemical Geology 262, 57-77.

Dawson, J.B., 1980. Kimberlites and their xenoliths. Springer Science & Business Media.

Day, J.M., Brandon, A.D., Walker, R.J., 2016. Highly siderophile elements in Earth, Mars, the Moon, and asteroids. Reviews in Mineralogy and Geochemistry 81, 161-238.

Fiorentini, M.L., Barnes, S.J., Lesher, C.M., Heggie, G.J., Keays, R.R., Burnham, O.M., 2010a. Platinum group element geochemistry of mineralized and nonmineralized komatiites and basalts. Economic Geology 105, 795-823.

Fiorentini, M.L., Barnes, S.J., Maier, W.D., Burnham, O.M., Heggie, G., 2010b. Global variability in the platinum-group element contents of komatiites. Journal of Petrology 52, 83-112.

Foley, S.F., 2008. Rejuvenation and erosion of the cratonic lithosphere. Nature Geoscience 1, 503.

Foley, S.F., 2011. A reappraisal of redox melting in the Earth's mantle as a function of tectonic setting and time. Journal of Petrology 52, 1363-1391.

Foley, S.F., Pintér, Z., 2018. Primary Melt Compositions in the Earth's Mantle, Magmas Under Pressure. Elsevier, pp. 3-42.

Gan, T., Huang, Z., 2017. Platinum-group element and Re-Os geochemistry of lamprophyres in the Zhenyuan gold deposit, Yunnan Province, China: Implications for petrogenesis and mantle evolution. Lithos.

Giuliani, A., 2018. Insights into kimberlite petrogenesis and mantle metasomatism from a review of the compositional zoning of olivine in kimberlites worldwide. Lithos 312, 322-342.

Giuliani, A., Pearson, D.G., 2019. Kimberlites: from deep earth to diamond mines. Elements: An International Magazine of Mineralogy, Geochemistry, and Petrology 15, 377-380.

Giuliani, A., Phillips, D., Woodhead, J.D., Kamenetsky, V.S., Fiorentini, M.L., Maas, R., Soltys, A., Armstrong, R.A., 2015. Did diamond-bearing orangeites originate from MARID-veined peridotites in the lithospheric mantle? Nature communications 6, 6837.

González-Jiménez, J., Proenza, J., Gervilla, F., Melgarejo, J., Blanco-Moreno, J., Ruiz-Sánchez, R., Griffin, W., 2011. High-Cr and high-Al chromitites from the Sagua de Tánamo district, Mayarí-Cristal ophiolitic massif (eastern Cuba): Constraints on their origin from mineralogy and geochemistry of chromian spinel and platinum-group elements. Lithos 125, 101-121.

González-Jiménez, J.M., Roqué-Rosell, J., Jiménez-Franco, A., Tassara, S., Nieto, F., Gervilla, F., Baurier, S., Proenza, J.A., Saunders, E., Deditius, A.P., 2019. Magmatic platinum nanoparticles in metasomatic silicate glasses and sulfides from Patagonian mantle xenoliths. Contributions to Mineralogy and Petrology 174, 47.

Graham, S., Lambert, D., Shee, S., 2004. The petrogenesis of carbonatite, melnoite and kimberlite from the Eastern Goldfields Province, Yilgarn Craton. Lithos 76, 519-533.

Griffin, W., Begg, G., O'reilly, S.Y., 2013. Continental-root control on the genesis of magmatic ore deposits. Nature Geoscience 6, 905-910.

Griffin, W.L., Belousova, E.A., Shee, S.R., Pearson, N.J., O'reilly, S.Y., 2004. Archean crustal evolution in the northern Yilgarn Craton: U–Pb and Hf-isotope evidence from detrital zircons. Precambrian Research 131, 231-282.

Groves, D., Ridley, J., Bloem, E., Gebre-Mariam, M., Hagemann, S., Hronsky, J., Knight, J., McNaughton, N., Ojala, J., Vielreicher, R., 1995. Lode-gold deposits of the Yilgarn block: products of Late Archaean crustal-scale overpressured hydrothermal systems. Geological Society, London, Special Publications 95, 155-172.

Guice, G.L., McDonald, I., Hughes, H.S., Anhaeusser, C.R., 2019. An evaluation of element mobility in the Modderfontein ultramafic complex, Johannesburg: Origin as an Archaean ophiolite fragment or greenstone belt remnant? Lithos 332, 99-119.

Holwell, D.A., Fiorentini, M., McDonald, I., Lu, Y., Giuliani, A., Smith, D.J., Keith, M., Locmelis, M., 2019. A metasomatized lithospheric mantle control on the metallogenic signature of post-subduction magmatism. Nature communications 10, 1-10.

Hughes, H.S., McDonald, I., Faithfull, J.W., Upton, B.G., Loocke, M., 2016. Cobalt and precious metals in sulphides of peridotite xenoliths and inferences concerning their distribution according to geodynamic environment: a case study from the Scottish lithospheric mantle. Lithos 240, 202-227.

Hughes, H.S., McDonald, I., Goodenough, K.M., Ciborowski, T.J.R., Kerr, A.C., Davies, J.H., Selby, D., 2014. Enriched lithospheric mantle keel below the Scottish margin of the North Atlantic Craton: Evidence from the Palaeoproterozoic Scourie Dyke Swarm and mantle xenoliths. Precambrian Research 250, 97-126.

Hughes, H.S., McDonald, I., Loocke, M., Butler, I.B., Upton, B.G., Faithfull, J.W., 2017. Paradoxical co-existing base metal sulphides in the mantle: The multi-event record preserved in Loch Roag peridotite xenoliths, North Atlantic Craton. Lithos 276, 103-121.

Johnson, S., Sheppard, S., Rasmussen, B., Wingate, M., Kirkland, C., Muhling, J., Fletcher, I., Belousova, E., 2011. Two collisions, two sutures: punctuated pre-1950 Ma assembly of the West Australian Craton during the Ophthalmian and Glenburgh Orogenies. Precambrian Research 189, 239-262.

Johnson, S.P., Thorne, A., Tyler, I., Korsch, R., Kennett, B., Cutten, H., Goodwin, J., Blay, O., Blewett, R., Joly, A., 2013. Crustal architecture of the Capricorn Orogen, Western Australia and associated metallogeny. Australian Journal of Earth Sciences 60, 681-705.

Kargin, A., Nosova, A., Larionova, Y.O., Kononova, V., Borisovsky, S., Koval'chuk, E., Griboedova, I., 2014. Mesoproterozoic orangeites (Kimberlites II) of West Karelia: mineralogy, geochemistry, and Sr-Nd isotope composition. Petrology 22, 151-183.

Keays, R., 1982. Palladium and iridium in komatiites and associated rocks: application to petrogenetic problems. Komatiites, 435-458.

Kent, A.J., Cassidy, K.F., Mark Fanning, C., 1996. Archean gold mineralization synchronous with the final stages of cratonization, Yilgarn Craton, Western Australia. Geology 24, 879-882.

Kepezhinskas, P., Defant, M.J., 2001. Non-chondritic Pt/Pd ratios in arc mantle xenoliths: Evidence for platinum enrichment in depleted island-arc mantle sources. Geology 29, 851-854.

Kirkland, C., Spaggiari, C., Pawley, M., Wingate, M., Smithies, R., Howard, H., Tyler, I., Belousova, E.A., Poujol, M., 2011. On the edge: U–Pb, Lu–Hf, and Sm–Nd data suggests reworking of the Yilgarn craton margin during formation of the Albany-Fraser Orogen. Precambrian Research 187, 223-247.

Kiviets, G.B., Phillips, D., Shee, S.R., Vercoe, S.C., Barton, E.S., Smith, C.B., Fourie, L.F., 1998. Ar/39 Ar dating of yimengite from the Turkey Well kimberlite, Australia: the oldest and the rarest, Seventh International kimberlite Conference. Extended Abstracts, Cape Town, pp. 432-433.

LaFlamme, C., Fiorentini, M.L., Lindsay, M.D., Bui, T.H., 2018. Atmospheric sulfur is recycled to the crystalline continental crust during supercontinent formation. Nature communications 9.

Le Vaillant, M., Barnes, S.J., Fiorentini, M.L., Santaguida, F., Törmänen, T., 2016. Effects of hydrous alteration on the distribution of base metals and platinum group elements within the Kevitsa magmatic nickel sulphide deposit. Ore Geology Reviews 72, 128-148.

Maier, W., O'Brien, H., Peltonen, P., Barnes, S.-J., 2017. Platinum-group element contents of Karelian kimberlites: Implications for the PGE budget of the sub-continental lithospheric mantle. Geochimica et Cosmochimica Acta 216, 358-371.

Maier, W.D., Barnes, S.-J., 2004. Pt/Pd and Pd/Ir ratios in mantle-derived magmas: a possible role for mantle metasomatism. South African Journal of Geology 107, 333-340.

Maier, W.D., Barnes, S.J., Campbell, I.H., Fiorentini, M.L., Peltonen, P., Barnes, S.-J., Smithies, R.H., 2009. Progressive mixing of meteoritic veneer into the early Earth's deep mantle. Nature 460, 620.

Maier, W.D., Peltonen, P., McDonald, I., Barnes, S.-J., Barnes, S.-J., Hutton, C., Viljoen, F., 2012. The concentration of platinum-group elements and gold in southern African and Karelian kimberlite-hosted mantle xenoliths: implications for the noble metal content of the Earth's mantle. Chemical Geology 302, 119-135.

Mavrogenes, J.A., O'Neill, H.S.C., 1999. The relative effects of pressure, temperature and oxygen fugacity on the solubility of sulfide in mafic magmas. Geochimica et Cosmochimica Acta 63, 1173-1180.

McDonald, I., De Wit, M., Smith, C., Bizzi, L., Viljoen, K., 1995. The geochemistry of the platinum-group elements in Brazilian and southern African kimberlites. Geochimica et Cosmochimica Acta 59, 2883-2903.

McDonough, W.F., Sun, S.-S., 1995. The composition of the Earth. Chemical geology 120, 223-253.

McNaughton, N.J., Mueller, A.G., Groves, D.I., 2005. The age of the giant Golden Mile deposit, Kalgoorlie, Western Australia: ion-microprobe zircon and monazite U-Pb geochronology of a synmineralization lamprophyre dike. Economic Geology 100, 1427-1440.

Mitchell, R.H., 1995. Kimberlites, orangeites, and related rocks. Springer Science & Business Media.

Mitchell, R.H., Giuliani, A., O'Brien, H., 2019. What is a kimberlite? Petrology and mineralogy of hypabyssal kimberlites. Elements: An International Magazine of Mineralogy, Geochemistry, and Petrology 15, 381-386.

Mole, D., Kirkland, C., Fiorentini, M., Barnes, S., Cassidy, K., Issac, C., Belousova, E., Hartnady, M., Thebaud, N., 2019. Time-space evolution of an archean craton: A Hf-isotope window into continent formation. Earth-Science Reviews.

Mole, D.R., Fiorentini, M.L., Cassidy, K.F., Kirkland, C.L., Thebaud, N., McCuaig, T.C., Doublier, M.P., Duuring, P., Romano, S.S., Maas, R., Belousova, E.A., Barnes, S.J., Miller, J., 2013. Crustal evolution, intra-cratonic architecture and the metallogeny of an Archaean craton. Geological Society, London, Special Publications 393, 23-80.

Mole, D.R., Fiorentini, M.L., Thebaud, N., Cassidy, K.F., McCuaig, T.C., Kirkland, C.L., Romano, S.S., Doublier, M.P., Belousova, E.A., Barnes, S.J., Miller, J., 2014. Archean komatiite volcanism controlled by the evolution of early continents. Proc Natl Acad Sci U S A 111, 10083-10088.

Mole, D.R., Fiorentini, M.L., Thebaud, N., McCuaig, T.C., Cassidy, K.F., Kirkland, C.L., Wingate, M.T.D., Romano, S.S., Doublier, M.P., Belousova, E.A., 2012. Spatio-temporal constraints on lithospheric development in the southwest–central Yilgarn Craton, Western Australia. Australian Journal of Earth Sciences 59, 625-656.

Mungall, J.E., Brenan, J.M., 2014. Partitioning of platinum-group elements and Au between sulfide liquid and basalt and the origins of mantle-crust fractionation of the chalcophile elements. Geochimica et Cosmochimica Acta 125, 265-289.

Myers, J.S., 1993. Precambrian history of the West Australian craton and adjacent orogens. Annual Review of Earth and Planetary Sciences 21, 453-485.

Myers, J.S., 1995. The generation and assembly of an Archaean supercontinent: evidence from the Yilgarn craton, Western Australia. Geological Society, London, Special Publications 95, 143-154.

Nelson, D., Myers, J., Nutman, A., 1995. Chronology and evolution of the Middle Proterozoic Albany-Fraser Orogen, Western Australia. Australian Journal of Earth Sciences 42, 481-495.

Nemchin, A., Pidgeon, R., Wilde, S., 1994. Timing of Late Archaean granulite facies metamorphism in the southwestern Yilgarn Craton of Western Australia: evidence from U ・ Pb ages of zircons fro mafic granulites. Precambrian Research 68, 307-321.

Nowell, G., Pearson, D., Bell, D., Carlson, R., Smith, C., Kempton, P., Noble, S., 2004. Hf isotope systematics of kimberlites and their megacrysts: new constraints on their source regions. Journal of Petrology 45, 1583-1612.

Nutman, A.P., Bennett, V.C., Kinny, P.D., Price, R., 1993. Large-scale crustal structure of the Northwestern Yilgarn Craton, western Australia: Evidence from Nd isotopic data and zircon geochronology. Tectonics 12, 971-981.

Occhipinti, S., Hocking, R., Lindsay, M., Aitken, A., Copp, I., Jones, J., Sheppard, S., Pirajno, F., Metelka, V., 2017. Paleoproterozoic basin development on the northern Yilgarn Craton, Western Australia. Precambrian Research 300, 121-140.

Orozco-Garza, A., Dostal, J., Keppie, J.D., Paz-Moreno, F.A., 2013. Mid-Tertiary (25–21Ma) lamprophyres in NW Mexico derived from subduction-modified subcontinental lithospheric mantle in an extensional backarc environment following steepening of the Benioff zone. Tectonophysics 590, 59-71.

Pandey, A., Rao, N.C., Chakrabarti, R., Pandaj, P., Pandit, D., Pandey, R., Sahoo, S., 2018. Post-collisional calc-alkaline lamprophyres from the Kadiri greenstone belt: Evidence for the Neoarchean convergence-related evolution of the Eastern Dharwar Craton and its schist belts. Lithos 320, 105-117.

Pawley, M., Romano, S., Hall, C., Wyche, S., Wingate, M., 2007. The Yamarna Shear Zone: a new terrane boundary in the north eastern Yilgarn Craton. Geological Survey of Western Australia, Annual Review 2008, 26-32.

Pawley, M.J., Wingate, M.T.D., Kirkland, C.L., Wyche, S., Hall, C.E., Romano, S.S., Doublier, M.P., 2012. Adding pieces to the puzzle: episodic crustal growth and a new terrane in the northeast Yilgarn Craton, Western Australia. Australian Journal of Earth Sciences 59, 603-623.

Pearson, D.G., Woodhead, J., Janney, P.E., 2019. Kimberlites as geochemical probes of Earth's mantle. Elements: An International Magazine of Mineralogy, Geochemistry, and Petrology 15, 387-392.

Perring, C.S., 1989. The Significance of" porphyry" Intrusions to Archaean Gold Mineralization in the Norseman-Wiluna Belt of Western Australia. University of Western Australia.

Perring, C.S., Rock, N.M., Golding, S.D., Roberts, D.E., 1989. Criteria for the recognition of metamorphosed or altered lamprophyres: a case study from the Archaean of Kambalda, Western Australia. Precambrian Research 43, 215-237.

Pidgeon, R.T., Wilde, S.A., 1990. The distribution of 3.0 Ga and 2.7 Ga volcanic episodes in the Yilgarn Craton of Western Australia. Precambrian Research 48, 309-325.

Pisarevsky, S.A., De Waele, B., Jones, S., Söderlund, U., Ernst, R.E., 2015. Paleomagnetism and U–Pb age of the 2.4 Ga Erayinia mafic dykes in the south-western Yilgarn, Western Australia: Paleogeographic and geodynamic implications. Precambrian Research 259, 222-231.

Robey, J., Bristow, J., Marx, M., Joyce, J., Danchin, R., Arnott, F., 1983. Alkaline ultrabasic dikes near Norseman, Western Australia. Kimberlites and Related Rocks 1, 383-391.

Roche, L., Korhonen, F., Johnson, S., Wingate, M., Hancock, E., Dunkley, D., Zi, J.-W., Rasmussen, B., Muhling, J., Occhipiniti, S., 2017. The evolution of a Precambrian arc-related granulite facies gold deposit: Evidence from the Glenburgh deposit, Western Australia. Precambrian Research 290, 63-85.

Rock, N., 1984. Nature and origin of calc-alkaline lamprophyres: minettes, vogesites, kersantites and spessartites. Transactions of the Royal Society of Edinburgh: Earth Sciences 74, 193-227.

Rock, N., 1986. The nature and origin of ultramafic lamprophyres: alnöites and allied rocks. Journal of Petrology 27, 155-196.

Rock, N.M.S., 1991. Lamprophyres. Springer Science & Business Media.

Said, N., Kerrich, R., 2009. Geochemistry of coexisting depleted and enriched Paringa Basalts, in the 2.7 Ga Kalgoorlie Terrane, Yilgarn Craton, Western Australia: evidence for a heterogeneous mantle plume event. Precambrian Research 174, 287-309.

Saunders, J.E., Pearson, N.J., O'Reilly, S.Y., Griffin, W.L., 2018. Gold in the mantle: A global assessment of abundance and redistribution processes. Lithos 322, 376-391.

Scott-Smith, B.H., Nowicki, T.E., Russell, J.K., Webb, K.J., Mitchell, R.H., Hetman, C.M., Robey, J.V.A., 2018. A Glossary of kimberlite and related rocks. Scott-Smith Petrology Inc.

Selvaraja, V., Caruso, S., Fiorentini, M.L., LaFlamme, C.K., Bui, T.-H., 2017a. Atmospheric sulfur in the orogenic gold deposits of the Archean Yilgarn Craton, Australia. Geology 45, 691-694.

Selvaraja, V., Fiorentini, M.L., LaFlamme, C.K., Wing, B.A., Bui, T.-H., 2017b. Anomalous sulfur isotopes trace volatile pathways in magmatic arcs. Geology 45, 419-422.

Shee, S.R., Vercoe, S.C., Wyatt, B.A., Hwang, P.H., Campbell, A.N., Colgan, E.A., 1999. Discovery and geology of the Nabberu kimberlite province, Western Australia, Proceedings of the VIIth International Kimberlite Conference, pp. 764-787.

Sheppard, S., Fletcher, I.R., Rasmussen, B., Zi, J.-W., Muhling, J.R., Occhipinti, S.A., Wingate, M.T., Johnson, S.P., 2016. A new Paleoproterozoic tectonic history of the eastern Capricorn Orogen, Western Australia, revealed by U–Pb zircon dating of micro-tuffs. Precambrian Research 286, 1-19.

Smirnov, A.V., Evans, D.A., Ernst, R.E., Söderlund, U., Li, Z.-X., 2013. Trading partners: Tectonic ancestry of southern Africa and western Australia, in Archean supercratons Vaalbara and Zimgarn. Precambrian Research 224, 11-22.

Smithies, R., Lu, Y., Kirkland, C., Cassidy, K.F., Champion, D.C., Burley, L., De Paoli, M., Sapkota, J., 2018a. A New Look at Lamprophyres and Sanukitoids and Their Relationship to the Black Flag Group and Gold Prospectivity. Geological Survey of Western Australia.

Smithies, R.H., Ivanic, T.J., Lowrey, J.R., Morris, P.A., Barnes, S.J., Wyche, S., Lu, Y.-J., 2018b. Two distinct origins for Archean greenstone belts. Earth and Planetary Science Letters 487, 106-116.

Soder, C., Romer, R.L., 2018. Post-collisional potassic–ultrapotassic magmatism of the Variscan Orogen: implications for mantle metasomatism during continental subduction. Journal of Petrology 59, 1007-1034.

Spaggiari, C., Kirkland, C., Smithies, R., Occhipinti, S., Wingate, M., 2014. Geological framework of the Albany–Fraser Orogen, Albany-Fraser Orogen seismic and magnetotelluric (MT) workshop 2014: Extended abstracts: Geological Survey of Western Australia Volume Record, pp. 12-27.

Spaggiari, C.V., Kirkland, C.L., Smithies, R.H., Wingate, M., Belousova, E.A., 2015. Transformation of an Archean craton margin during Proterozoic basin formation and magmatism: The Albany–Fraser Orogen, Western Australia. Precambrian Research 266, 440-466.

Swager, C., Goleby, B., Drummond, B., Rattenbury, M., Williams, P., 1997. Crustal structure of granite-greenstone terranes in the Eastern Goldfields, Yilgarn Craton, as revealed by seismic reflection profiling. Precambrian Research 83, 43-56.

Swager, C., Witt, W., Griffin, T., Ahmat, A., Hunter, W., McGoldrick, P., Wyche, S., 1992. Late Archaean granite-greenstones of the Kalgoorlie Terrane, Yilgarn Craton, Western Australia. The Archaean: terrains, processes and metallogeny 22, 107-122.

Tappe, S., Brand, N.B., Stracke, A., van Acken, D., Liu, C.-Z., Strauss, H., Wu, F.-Y., Luguet, A., Mitchell, R.H., 2017. Plates or plumes in the origin of kimberlites: U/Pb perovskite and Sr-Nd-Hf-Os-CO isotope constraints from the Superior craton (Canada). Chemical Geology 455, 57-83.

Tappe, S., Foley, S.F., Jenner, G.A., Kjarsgaard, B.A., 2005. Integrating ultramafic lamprophyres into the IUGS classification of igneous rocks: rationale and implications. Journal of Petrology 46, 1893-1900.

Tappe, S., Foley, S.F., Kjarsgaard, B.A., Romer, R.L., Heaman, L.M., Stracke, A., Jenner, G.A., 2008. Between carbonatite and lamproite—diamondiferous Torngat ultramafic lamprophyres formed by carbonate-fluxed melting of cratonic MARID-type metasomes. Geochimica et Cosmochimica Acta 72, 3258-3286.

Tassara, S., González-Jiménez, J.M., Reich, M., Saunders, E., Luguet, A., Morata, D., Grégoire, M., van Acken, D., Schilling, M.E., Barra, F., 2018. Highly siderophile elements mobility in the subcontinental lithospheric mantle beneath southern Patagonia. Lithos 314, 579-596.

Tassara, S., González-Jiménez, J.M., Reich, M., Schilling, M.E., Morata, D., Begg, G., Saunders, E., Griffin, W.L., O'Reilly, S.Y., Grégoire, M., 2017. Plume-subduction interaction forms large auriferous provinces. Nature Communications 8.

Tassara, S., Reich, M., Konecke, B.A., González-Jiménez, J.M., Simon, A.C., Morata, D., Barra, F., Fiege, A., Schilling, M.E., Alexandre, C., 2020. Unraveling the Effects of Melt–Mantle Interactions on the Gold Fertility of Magmas.

Taylor, W.R., Rock, N.M., Groves, D.I., Perring, C.S., Golding, S.D., 1994. Geochemistry of Archean shoshonitic lamprophyres from the Yilgarn Block, Western Australia: Au abundance and association with gold mineralization. Applied geochemistry 9, 197-222.

van der Meer, Q.H., Storey, M., Scott, J.M., Waight, T.E., 2016. Abrupt spatial and geochemical changes in lamprophyre magmatism related to Gondwana fragmentation prior, during and after opening of the Tasman Sea. Gondwana Research 36, 142-156.

Vielreicher, N., Groves, D., McNaughton, N., Fletcher, I., 2015. The timing of gold mineralization across the eastern Yilgarn craton using U–Pb geochronology of hydrothermal phosphate minerals. Mineralium Deposita 50, 391-428.

Wang, X.-C., Li, Z.-X., Li, J., Pisarevsky, S.A., Wingate, M.T., 2014. Genesis of the 1.21 Ga Marnda Moorn large igneous province by plume–lithosphere interaction. Precambrian Research 241, 85-103.

Wang, Z., Cheng, H., Zong, K., Geng, X., Liu, Y., Yang, J., Wu, F., Becker, H., Foley, S., Wang, C.Y., 2020. Metasomatized lithospheric mantle for Mesozoic giant gold deposits in the North China craton. Geology 48, 169-173.

Webster, J.D., Piccoli, P.M., 2015. Magmatic apatite. A powerful, yet deceptive, mineral. Elements 11, 177-182.

Wilde, S.A., Middleton, M.F., Evans, B.J., 1996. Terrane accretion in the southwestern Yilgarn Craton: evidence from a deep seismic crustal profile. Precambrian Research 78, 179-196.

Wingate, M.T., Pirajno, F., Morris, P.A., 2004. Warakurna large igneous province: A new Mesoproterozoic large igneous province in west-central Australia. Geology 32, 105-108.

Woodhead, J., Hergt, J., Giuliani, A., Maas, R., Phillips, D., Pearson, D.G., Nowell, G., 2019. Kimberlites reveal 2.5-billion-year evolution of a deep, isolated mantle reservoir. Nature 573, 578-581.

Wyche, S., Kirkland, C., Riganti, A., Pawley, M., Belousova, E., Wingate, M., 2012. Isotopic constraints on stratigraphy in the central and eastern Yilgarn Craton, Western Australia. Australian Journal of Earth Sciences 59, 657-670.

Yaxley, G.M., Berry, A., Rosenthal, A., Woodland, A., Paterson, D., 2017. Redox preconditioning deep cratonic lithosphere for kimberlite genesis–evidence from the central Slave Craton. Scientific reports 7, 1-10.

Zhang, H.-F., Zhou, M.-F., Sun, M., Zhou, X.-H., 2010. The origin of Mengyin and Fuxian diamondiferous kimberlites from the North China Craton: implication for Palaeozoic subducted oceanic slab–mantle interaction. Journal of Asian Earth Sciences 37, 425-437.

Sample	Age	Alteration Index*	Region	Au (ppb)	Ir	Pd	Pt	Rh	Ru	$(Pd/Ir)_N$	$(Pd/Pt)_N$	S (
Calc-alkaline lamprophyres (CAL) within the EGS												
128198	~2684-2640 Ma[1, 2]	I	Leonora	13.81	0.33	2.70	3.07	0.26	0.26	4.0	0.9	0
128181	~2684-2640 Ma[1, 2]	III	Leonora	5.30	0.09	1.94	1.56	0.16	<0.08	10.6	1.3	0
128186	~2684-2640 Ma[1, 2]	II	New Celebration	7.41	0.06	1.59	2.72	0.14	<0.08	13.1	0.6	0
128210	~2684-2640 Ma[1, 2]	I	New Celebration	6.61	0.05	1.45	2.59	0.13	<0.08	14.3	0.6	0
128200	~2684-2640 Ma[1, 2]	III	New Celebration	5.70	0.11	1.42	2.03	0.26	0.09	6.4	0.7	<
128178	~2684-2640 Ma[1, 2]	II	Murrin	4.87	0.20	2.96	3.34	0.31	<0.08	7.3	0.9	0
128191	~2684-2640 Ma[1, 2]	I	Minerie	4.53	0.05	0.76	1.59	0.09	<0.08	7.5	0.5	0
128182	~2684-2640 Ma[1, 2]	I	Minerie	3.49	0.07	2.32	4.05	0.11	<0.08	16.3	0.6	0
128193	~2684-2640 Ma[1, 2]	I	Minerie	6.46	0.19	3.28	3.62	0.30	<0.08	8.8	1.0	0
128180	~2684-2640 Ma[1, 2]	II	Minerie	0.40	0.07	1.69	1.74	0.14	<0.08	11.9	1.0	0
JD3-1	~2684-2640 Ma[1, 2]	II	Jundee	2.44	0.24	4.72	4.31	0.31	0.43	9.7	1.2	0
JD4-1	~2684-2640 Ma[1, 2]	III	Jundee	0.73	0.04	2.16	0.95	0.05	<0.08	26.6	2.4	0
JD1	~2684-2640 Ma[1, 2]	III	Jundee	0.51	0.12	2.78	2.52	0.19	0.11	11.4	1.2	0
JD3-2a	~2684-2640 Ma[1, 2]	III	Jundee	<0.4	0.08	1.93	1.33	0.09	0.16	11.9	1.6	0
Z36408	~2684-2640 Ma[1, 2]	II	Kambalda	2.50	0.17	1.86	4.30	0.26	0.29	5.4	0.5	<
Z36413	~2684-2640 Ma[1, 2]	II	Kambalda	0.50	0.17	1.16	2.82	0.28	0.26	3.4	0.4	0
Z36406	~2684-2640 Ma[1, 2]	I	Kambalda	0.40	0.19	1.54	2.27	0.30	0.31	4.0	0.7	<
Z27949	~2684-2640 Ma[1, 2]	II	Kambalda	1.20	0.05	1.15	1.44	0.09	<0.08	11.3	0.9	0
Z18500	~2684-2640 Ma[1, 2]	I	Kambalda	<0.4	0.03	0.81	0.90	0.05	<0.08	13.3	1.0	<
Ultramafic lamprophyres (UML) within the EGS												
Lara1	~2025 Ma[3]	II	Lara	1.00	0.12	1.02	0.85	0.08	0.17	4.2	1.3	0
128207	~2025 Ma[3]	II	Lara	0.90	0.08	0.89	0.73	0.07	0.14	5.5	1.3	0
Melita1	~2025 Ma[3]	II	Melita	1.10	1.28	4.42	3.26	0.41	3.56	1.7	1.5	0
Melita3	~2025 Ma[3]	III	Melita	0.60	0.45	0.91	0.89	0.15	0.80	1.0	1.1	0
AKB-1	~2025 Ma[3]	I	Melrose Akbar	2.66	0.04	0.20	0.72	<0.04	<0.08	2.5	0.3	0
AN01	~863 Ma[4]	I	Norseman	9.80	0.10	0.73	0.87	0.07	0.24	3.6	0.9	0
Carbonatites within the EGS												
MW2	~2025 Ma[3]	II	Mt. Weld	<0.4	0.11	0.76	0.73	0.05	<0.08	3.4	1.1	0
CH04-5	~2025 Ma[3]	I	Mt. Weld	<0.4	0.01	<0.12	<0.17	<0.04	<0.08	N/A	N/A	0
CH04-3	~2025 Ma[3]	I	Mt. Weld	0.50	0.01	<0.12	<0.17	<0.04	<0.08	N/A	N/A	0
128211	~2025 Ma[3]	I	Mt. Weld	3.71	0.08	0.30	1.19	<0.04	0.10	1.8	0.3	0
Orangeites in the Earaheedy Basin												
BJ-5-5	~1406 Ma[5]	I	Bulljah	<0.4	0.60	0.90	<0.17	0.13	0.65	0.7	N/A	0
BJ-5-1	~1406 Ma[5]	I	Bulljah	3.76	0.33	0.21	1.47	0.09	0.67	0.3	0.2	0
N#92-7	~1700-1900 Ma[6]	III	Nabberu	<0.4	1.09	0.16	0.55	0.22	2.10	0.1	0.3	<
N#92-5	~1700-1900 Ma[6]	III	Nabberu	<0.4	0.43	0.24	0.24	0.09	0.77	0.3	1.1	0

Kimberlites within the EGS

Teutonic 1	~2025 Ma[3]	III	Teutonic Bore	<0.4	0.01	<0.12	<0.17	<0.04	<0.08	N/A	N/A	0
Turkey2	~2025 Ma[3]	III	Turkey	<0.4	1.25	4.82	2.80	0.41	3.14	1.9	1.8	0

Note: alteration index I = fresh; II = moderately altered; III = highly altered (see main text for details).

*data of CAL samples from Choi et al. (2020), and of UML, carbonatites, orangeites and kimberlites from Choi (2020).

Details about the alteration index are described in the main text.

[1]McNaughton et al. (2005), [2]Perring et al. (1989), [3]Graham et al. (2004), [4]Robey et al. (1989), [5]Choi (2020), and [6]Shee et al. (1999).

Declaration of interests

☒ The authors declare that they have no known competing financial interests or personal relationships that could have appeared to influence the work reported in this paper.

☐The authors declare the following financial interests/personal relationships which may be considered as potential competing interests:

Highlights

- New PGE-Au of calc-alkaline/alkaline ultramafic magmas in the Yilgarn Craton
- PGE signature of Proterozoic UML reflects sulfide retention in convective mantle
- PGE signature of Archean CAL reflects incongruent melting of mantle sulfides
- Subduction-related volatile flux as first-order control on Archean Au endowment